CHAPTER 10

CHEMICAL POTENTIAL OF PHOTONS AND ITS IMPLICATIONS FOR CONTROLLING RADIATIVE HEAT TRANSFER

***Bo Zhao*[*] & Shanhui Fan*[*]**

Department of Electrical Engineering, Stanford University, Stanford, CA

[*]Address all correspondence to: Bo Zhao, E-mail: bzhao89@stanford.edu; or Shanhui Fan, E-mail: shanhui@stanford.edu

In conventional photon-based heat transfer, one typically assumes that the chemical potential of photons is zero. On the other hand, when a semiconductor is under external biases, the photons with energy above the semiconductor bandgap can exhibit a nonzero chemical potential that is proportional to the applied voltage. The presence of such nonzero chemical potential points to the abilities to drastically enhance the power density of photon-based heat flow, to electronically control photon-based heat transfer, and to construct photon-based heat engines for energy harvesting and solid-state cooling. In this review, we discuss basic concepts and applications of chemical potential of photons in controlling radiative heat transfer.

KEY WORDS: *photon chemical potential, energy harvesting, solid-state cooling, semiconductor, optoelectronics*

1. INTRODUCTION

Photons represent one of the most important heat carriers. For two objects with different temperatures separated by a vacuum, photon-based heat transfer, i.e., radiative heat transfer, is the only mechanism for them to exchange energy. Since photons do not interact with each other in a vacuum, the thermodynamic state of the emitted photons is determined by the thermodynamic state of the emitting body.[1–3] In the conventional description of radiative heat transfer, the emitting body is assumed to be at thermal equilibrium as characterized by a temperature, T. Consequently, the chemical potential of photon is zero.[2] The photon number in a mode at an angular frequency ω can be described by[2]

$$n = \frac{1}{\exp(\hbar\omega/k_B T) - 1} \tag{1}$$

where T is the temperature, k_B is the Boltzmann constant, and $\hbar$ is the reduced Planck constant.

On the other hand, if the emitting body is not at thermal equilibrium, the photon number distribution may not be described by Eq. (1). As a specific example, consider a semiconductor photodiode under external bias. Suppose the semiconductor is in quasi-equilibrium, i.e., the electrons in the conduction and valence bands are separately in equilibrium themselves, but the chemical potential of these two types of electrons has a nonzero

ISSN: 1049–0787; ISBN: 978–1–56700–500–4/20/$35.00 + $00.00

© 2020 by Begell House, Inc. www.begellhouse.com

NOMENCLATURE

Symbol	Description
c	speed of light in vacuum, m/s
E_c	conduction band edge, eV
E_{Fn}	quasi-Fermi level of the electrons in the conduction band, eV
E_{Fp}	quasi-Fermi level of the electrons in the valance band, eV
E_v	valance band edge, eV
F	net photon flux, 1/s/m^2
F_s	electron-hole pair generation rate due to irradiance, 1/s/m^2
F_d	radiative recombination rate of the diode, 1/s/m^2
f	spectral photon flux, s/rad/m^2
G	Gibbs free energy, J
$\hbar$	reduced Planck constant, J·s
I	current density, A/m^2
j	fluctuation current density, A/m^2
k_B	Boltzmann constant, J/K
k_x	wavevector in the x direction, 1/m
k_y	wavevector in the y direction, 1/m
N	N-region of a diode or nonradiative recombination or generation rate, 1/s/m^2
N_i	particle number of species i
n	refractive index or photon number in a mode
P	P-region of a diode or pressure, Pa
Q	heat flux, W/m^2
Q_c	cooling power, W/m^2
q	unit electrical charge, C, or spectral heat flux, W·s/rad/m^2
R	reflectance or resistance, Ω
S	entropy, J/K
T	temperature, K
V	voltage or volume, V or m^3
W	electrical power density, W/m^2
$\mathbf{x}$	position vector, m

Greek symbols

Symbol	Description
ε_0	vacuum permittivity
ε_e	dielectric function
ε	spectral directional emissivity
η	quantum efficiency
Θ	energy in a mode, J
μ	chemical potential, eV
ω	angular frequency, rad/s

Subscripts

Symbol	Description
app	apparent
c	conduction or cooling
d	diode
EQE	external quantum efficiency
EXT	light extraction
e	electron
g	bandgap
h	hole
IQE	internal quantum efficiency
i	species of particle
LED	light-emitting diode
oc	open circuit
PV	photovoltaic cell
ph	photon
rad	radiant temperature
s	source of incoming photons
t	threshold

difference qV, where q is the unit electrical charge. Since the photons are actively interacting with the electrons in the system, they can acquire a nonzero chemical potential, and the photon number in a mode can be described by the Bose-Einstein distribution[4–8]

$$n = \frac{1}{\exp\left[(\hbar\omega - qV)/k_B T\right] - 1} \tag{2}$$

The chemical potential difference qV between the electrons in the conduction and valence band thus becomes the chemical potential of photons.

A direct consequence of this chemical potential is that the spectral power density of the radiation can be significantly enhanced (when V is positive) or suppressed (when V is negative) compared to the thermal equilibrium case as described by Eq. (1); therefore, one could actively apply a bias on a diode to manipulate radiative heat transfer.[9] Moreover, photon gas in the diode can also develop a chemical potential in the presence of external incident light. The concept of chemical potential of photons is therefore useful to describe the process of energy harvesting.[4]

The concept of the chemical potential of photons has a long history. In 1982, Wurfel[1] published an influential paper that explicitly introduced the concept of the chemical potential of photons and discussed its various consequences in the light-emitting processes of semiconductors. This concept has also been separately introduced by Landsberg.[6] The theoretical analysis of solar cells, including the Shockley-Queisser analysis,[4,6–8] and the analysis of light-emitting diodes (LEDs)[10] can both be presented using the concept of the chemical potential of photons. With the recent developments in nanotechnologies and optoelectronics, especially the advances in near-field heat transfer[11–21] and continuously improving semiconductor devices,[10,22–25] there are renewed interests in exploring and further developing this concept. Motivated by these recent developments, in this chapter we review the fundamental concept of photon chemical potential and recent advances of utilizing photon chemical potential in semiconductor photodiodes for controlling radiative heat transfer and for constructing various photon-based heat engines and heat pumps.

The arrangement of the remaining part of this chapter is outlined in the following. In Section 2, we present the fundamental concept of photon chemical potential. In Sections 3 and 4, we discuss some of the device ideas based on the concept of photon chemical potential. Specifically, in Section 3, we review solid-state coolers based on semiconductor photodiodes. In Section 4, we review novel power generation techniques, including the negative-illumination power harvester and thermophotonic power harvester. We summarize and conclude in Section 5.

2. FUNDAMENTALS OF PHOTON CHEMICAL POTENTIAL

2.1 Photon Chemical Potential in Semiconductor Diodes

We consider a semiconductor photodiode under external bias. In Fig. 1, we show a typical energy diagram for the active region of such a diode under a bias voltage V across the active region that is positive. E_c and E_v are the conduction and valance band edges, respectively. We assume that the active region is in quasi-equilibrium, i.e., the electrons in the conduction and valence bands are each in equilibrium with themselves in the same band, but electrons in different bands are not in equilibrium. We can then define the quasi-Fermi levels E_{Fn} and E_{Fp} for the electrons in conduction and valance bands, respectively. The

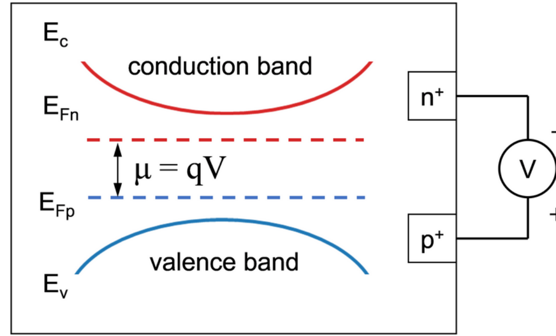

FIG. 1: Energy diagram for the active region of a semiconductor under positive bias. E_c and E_v are the conduction and valance band edges, respectively. E_{Fn} and E_{Fp} are the quasi-Fermi levels for the electrons in conduction and valance bands, respectively.

presence of the bias results in separation of the quasi-Fermi levels, i.e., $qV = E_{Fn} - E_{Fp}$. The chemical potentials of the electrons (μ_e) and holes (μ_h) are E_{Fn} and $-E_{Fp}$, respectively.

In such a semiconductor photodiode, the interaction between the electrons (e), holes (h), and photons (ph) can be treated as a chemical reaction[5]

$$e + h \rightarrow ph \tag{3}$$

At steady state, the system is in equilibrium and, therefore, the Gibbs free energy, G, should be minimized,[5] i.e.,

$$dG = -SdT + VdP + \sum_i \mu_i dN_i = 0 \tag{4}$$

where S, T, V, P are the entropy, temperature, volume, and pressure of the system, respectively, and μ_i and N_i are the chemical potential and the particle number of species i, where $i =$ electron (e), hole (h), and photons (ph). Assuming that the system is maintained at a constant P and T, we have[4,8]

$$\mu_e dN_e + \mu_h dN_h + \mu_{ph} dN_{ph} = 0 \tag{5}$$

From Eq. (3), the creation of a single photon comes from annihilation of a conduction-band electron and addition of a valence-band electron (or annihilation of a hole), i.e., $-dN_e = -dN_h = dN_{ph}$; therefore, from Eq. (5) we obtain[8]

$$\mu_{ph} = \mu_e + \mu_h = E_{Fn} - E_{Fp} = qV \tag{6}$$

Therefore, photons in this system possess a chemical potential of $\mu_{ph} = qV$. The expected photon number in a mode can be obtained by the Bose-Einstein distribution shown in Eq. (2). The energy in a mode is

$$\Theta(\omega, T, V) = \frac{\hbar\omega}{\exp[(\hbar\omega - qV)/k_B T] - 1} \tag{7}$$

The standard thermal radiation thus corresponds to the case when $\mu_{ph} = 0$. With Eq. (7), we can now describe both thermal and nonthermal radiation.

2.2 Fluctuation-Dissipation Theorem

In Section 2.1, we discussed the concept of chemical potential of photon. Here, we use this concept to describe the emission from a semiconductor diode [Fig. 2(a)] as well as heat transfer between a diode and another radiative body [Fig. 2(b)]. In describing heat transfer, we differentiate the near- and far-field regimes, depending on whether the distance between the two bodies is significantly above the relevant wavelength or not. Typically, one expects significant enhancement of the power density in the near-field regime.

The scenarios in both Figs. 2(a) and 2(b) can be treated by modifying the standard fluctuational electrodynamics formalism. In the standard formalism,[26] the emission or heat transfer results from the energy flux generated by fluctuating dipoles. The strength of the fluctuation is set by the fluctuation-dissipation theorem. In the present case, within the diode, the autocorrelation function of fluctuation currents becomes[27]

$$\langle j_k(\mathbf{x}', \omega) j_n^*(\mathbf{x}'', \omega')\rangle = \begin{cases} \dfrac{4}{\pi}\omega\varepsilon_0 \mathrm{Im}(\varepsilon_e)\Theta(\omega, T, 0)\delta_{kn}\delta(\mathbf{x}' - \mathbf{x}'')\delta(\omega - \omega') \\ \qquad \omega \le \omega_g \\ \dfrac{4}{\pi}\omega\varepsilon_0 \mathrm{Im}(\varepsilon_e)\Theta(\omega, T, V)\delta_{kn}\delta(\mathbf{x}' - \mathbf{x}'')\delta(\omega - \omega') \\ \qquad \omega > \omega_g \end{cases} \tag{8}$$

where k and n denote the directions of polarization, $\mathbf{x}'$ and $\mathbf{x}''$ are position vectors, $\mathrm{Im}(\varepsilon_e)$ is the imaginary part of the dielectric function, ε_0 is the vacuum permittivity, and δ is the Dirac delta function. With this modification, one can then use the standard fluctuational electrodynamics formalism to compute the heat transfer between bodies with nonzero photon chemical potential. In all of Section 2, we consider the ideal case where there is no sub-bandgap absorption, i.e., $\mathrm{Im}(\varepsilon_e) = 0$ for $\omega < \omega_g$. The effect of sub-bandgap absorption will be discussed in Section 3.

We first consider the emission from a diode, as shown in Fig. 2(a). The energy flux Q emitted from the diode has the form

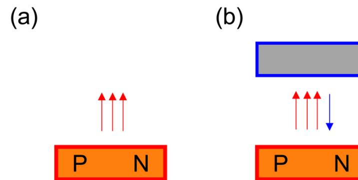

FIG. 2: A semiconductor diode (a) emitting to a zero-Kelvin vacuum and (b) going through radiative exchange with another radiative body

$$Q(T,V) = \int_{\omega_g}^{\infty} q(\omega,T,V)d\omega \tag{9}$$

where $q(\omega,T,V)$ is the spectral heat flux

$$q(\omega,T,V) = \frac{1}{8\pi^3}\int\int \varepsilon(\omega,k_x,k_y)\Theta(\omega,T,V)dk_x dk_y \tag{10}$$

In Eq. (10), $\varepsilon(\omega,k_x,k_y)$ is the spectral directional emissivity, k_x and k_y are the two parallel wavevector components. The photon flux is

$$F(T,V) = \int_{\omega_g}^{\infty} f(\omega,T,V)d\omega \tag{11}$$

where

$$f(\omega,T,V) = \frac{q(\omega,T,V)}{\hbar\omega} \tag{12}$$

is the spectral photon flux.

We then consider the heat transfer case between two emitting bodies, denoted as 1 and 2, as shown in Fig. 2(b). The net radiative heat flux is

$$Q = Q_1(T_1,V_1) - Q_2(T_2,V_2) \tag{13}$$

where

$$Q_1(T_1,V_1) = \int_{\omega_g}^{\infty} q_1(\omega,T_1,V_1)d\omega \tag{14}$$

and

$$Q_2(T_2,V_2) = \int_{\omega_g}^{\infty} q_2(\omega,T_2,V_2)d\omega \tag{15}$$

with the spectral heat flux given by

$$q_1(\omega,T_1,V_1) = \frac{1}{8\pi^3}\int\int \xi(\omega,k_x,k_y)\Theta(\omega,T_1,V_1)dk_x dk_y \tag{16}$$

and

$$q_2(\omega,T_2,V_2) = \frac{1}{8\pi^3}\int\int \xi(\omega,k_x,k_y)\Theta(\omega,T_2,V_2)dk_x dk_y \tag{17}$$

where $\xi(\omega,k_x,k_y)$ is the energy transmission coefficient summing over the two polarizations (with a maximum value of 2). Equation (16) describes the heat flux emitted by body 1; whereas, Eq. (17) describes the heat flux absorbed by body 1, which is due to the emission of body 2 and hence depends on the temperature and the chemical potential of body 2. The photon flux is

$$F = F_1(T_1,V_1) - F_2(T_2,V_2) \tag{18}$$

where

$$F_1(T_1, V_1) = \int_{\omega_g}^{\infty} \frac{q_1(\omega, T_1, V_1)}{\hbar\omega} d\omega \tag{19}$$

and

$$F_2(T_2, V_2) = \int_{\omega_g}^{\infty} \frac{q_2(\omega, T_2, V_2)}{\hbar\omega} d\omega \tag{20}$$

with

$$f_1(\omega, T_1, V_1) = \frac{q_1(\omega, T_1, V_1)}{\hbar\omega} \tag{21}$$

and

$$f_2(\omega, T_2, V_2) = \frac{q_2(\omega, T_2, V_2)}{\hbar\omega} \tag{22}$$

are the spectral photon fluxes for bodies 1 and 2, respectively.

Equations (10), (16), and (17) contain integration over k_x and k_y. The major difference between the far-field heat transfer and near-field heat transfer is that, for the far-field case, k_x and k_y are bounded by $k_x^2 + k_y^2 \leq \omega^2/c^2$, where c is the speed of light in vacuum; whereas for the near-field case, $k_x^2 + k_y^2 \leq +\infty$, i.e., k_x and k_y are unbounded. Since the integrated wavevector space is much larger in the near-field scenario, the spectral heat flux $q(\omega)$ can be greatly enhanced to significantly exceed the heat flux between far-field blackbodies. The spectral photon flux can also be enhanced accordingly.

We note that the near-field effect has been applied to enhance radiative heat transfer, i.e., two bodies with zero photon chemical potentials.[28–31] The same enhancement persists when the emitting bodies possess a nonzero photon chemical potential. Such an enhancement effect, in addition to increasing power density, may be also used to overcome some of the challenges related to light extraction or nonradiative recombination in semiconductors, as we discuss in Section 2.3.

2.3 Radiant Temperature

In both far- and near-field radiation of the diode, since typically $\hbar\omega_g \gg k_B T$, from Eqs. (10), (16), and (17), we see that the emission from a semiconductor is typically narrow banded near ω_g and has a bandwidth on the order of a few $k_B T$. For such a narrow band heat flux spectrum, the concept of radiant temperature of radiation[32] is very useful. The radiant temperature, T_{rad}, is defined by equating the spectral heat flux at the bandgap for a diode at a temperature T to that of a thermal body at a temperature T_{rad}, which results in the following:

$$T_{\text{rad}} = T \left(\frac{\hbar\omega_g}{\hbar\omega_g - qV} \right) \tag{23}$$

For a diode under positive bias, the radiant temperature of the above-bandgap radiation is higher than the temperature of the diode; whereas when the bias is negative, the radiant temperature is lower than the temperature of the diode. To illustrate the concept of radiant temperature, we show in Fig. 3 the spectral heat flux for a diode at 6×10^2 K with a bandgap of 0.5 eV under three different biases: $+0.25$, 0, and –0.25 V. For the 0 V case, the spectral

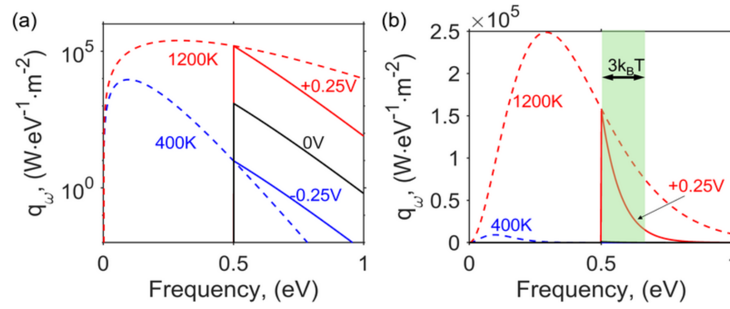

FIG. 3: Spectral power density from a semiconductor diode at 6×10^2 K under different bias in (a) logarithmic scale and (b) linear scale. The bandgap of the diode is 0.5 eV. The solid black, red, and blue lines are for the cases where the bias voltages are 0.25, 0, and –0.25 V, respectively. The two dashed lines in blue and red are for blackbodies at temperatures of 4×10^2 and 12×10^2 K, respectively. The emission from the semiconductor has a bandwidth of a few $k_B T$, as indicated by the green area in (b).

heat flux above the bandgap is identical to a blackbody at the same temperature. With a voltage of $+0.25$ V, the above-bandgap emission is greatly enhanced and it has the same spectral heat flux as a thermal emitter at the radiant temperature of 12×10^2 K (upper dashed curve in Fig. 3) at the bandgap. In contrast, when the diode is under a negative bias of –0.25 V, the above-bandgap emission is strongly suppressed and it has the same spectral flux as a thermal emitter at the radiant temperature of 4×10^2 K (lower dashed curve in Fig. 3). A relatively small change of the applied voltage can thus lead to a large change in the radiant temperature. The application of bias thus provides a way to manipulate the direction of radiation heat flow, as is discussed in detail in Section 2.4.

We note that, in the aforementioned discussion, the above-bandgap emissivity is assumed to be 1. For realistic semiconductors with a finite size, the absorptivity should vanish at the bandgap; hence, the line shape of the emission would be different from the idealized model previously used.[33,34] In detailed calculations of physical devices, these effects must be taken into account.

2.4 Detailed Balance of Semiconductor Diodes

In the aforementioned discussions, we considered the emission from a diode to vacuum. In addition to emission, the diode may absorb from other radiative bodies as sources of incoming photons, as Eq. (13) shows. Taking into account both the absorption and the emission processes, as well as the fact that the voltage bias is typically associated with an injected current, a diode can be described by a detailed balance equation[4]

$$F_s(V_s, T_s) - F_d(V, T) + N(0, T) - N(V, T) + \frac{I}{q} = 0 \tag{24}$$

where I/q is the rate at which electrons are injected in the diode, $F_s(V_s, T_s)$ is the rate of generation of electron-hole pairs due to irradiance form the sources; $N(0, T)$ is the rate

of nonradiative generation processes; $N(V,T)$ is the rate of nonradiative recombination processes; and $F_d(V,T)$ is the rate of radiative recombination in the diode. F_s and F_d are described by Eqs. (19) or (20).

2.5 Operation State of a Photodiode

The detailed balance equation [Eq. (24)] points to a rich set of effects in heat exchange between a diode and another emitting body, as shown in Fig. 4(a). On the basis of Eq. (24), assuming the diode has no nonradiative processes, we obtain

$$I = q \int_{\omega_g}^{\infty} \left[f_d\left(\omega, T, V\right) - f_s\left(\omega, T_s, 0\right) \right] d\omega \tag{25}$$

An additional equation of I and V can be obtained from the circuit law that describes the load or batteries attached to the diode. In this way, the current I and the voltage V of the diode can be obtained.

When the temperature of the emitting body is the same as the diode, i.e., $T = T_s$ in Eq. (24), in the absence of a voltage on the diode, the system is in thermal equilibrium and the current passing through the diode must be zero. The I–V curve therefore passes

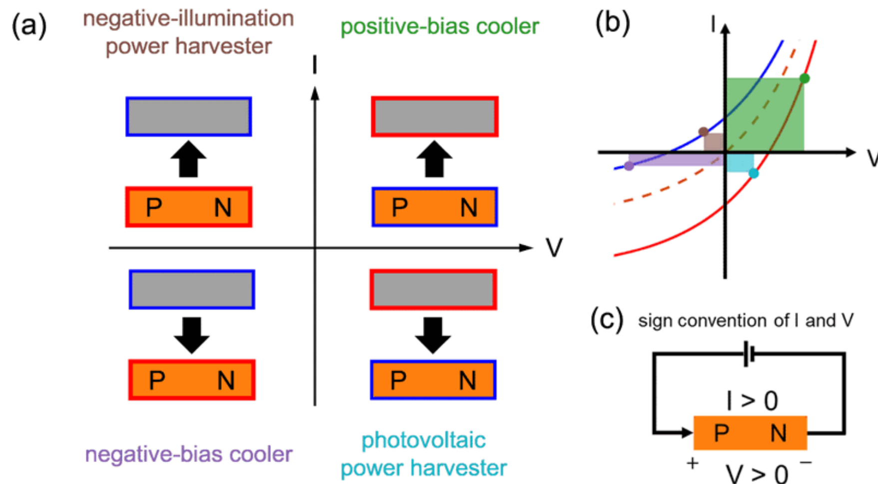

FIG. 4: (a) Four operation states of a photodiode facing a radiative thermal body. The color of the boundary of an object indicates whether the body is cold (blue boundary) or hot (red boundary). The thick arrows show the direction of the net radiative heat flux. The functionalities of the diode in the four quadrants are respectively positive-bias cooler (or electroluminescent refrigerator), negative-illumination power harvester (or thermoradiative cell), negative-bias cooler (or negative electroluminescent refrigerator), and photovoltaic power harvester. (b) The operation points of the four scenarios in (a) on the I–V curves. The shaded boxes are power consumption or production. (c) Sign convention of I and V.

through the origin, as shown by the dashed line in Fig. 4(b). When the temperature of the emitting body is higher than the diode, in the open circuit situation where $I = 0$, the incoming photon flux from the emitting body has to be balanced by the emitting photons from the diode. The diode needs to exhibit a positive open-circuit voltage. The I–V curve thus shifts to the right in the I–V plane such that the intercept point of the curve with the I-axis, which defines the short circuit current, moves downward, as shown by the lower solid curve in Fig. 4(b). With similar arguments, one can show that when the temperature of the emitting body is lower than the diode, the I–V curve shifts to the left, as shown by the upper solid curve in Fig. 4(b).

With our convention of the sign for the current and voltage, $P = IV$ describes the electric power injected to the diode, with $P < 0$ corresponding to the cases where the diode generates electric power. Within the I–V plane, the axes of $I = 0$ and $V = 0$ separate the plane into four quadrants. In the first and third quadrants, electric power is injected into the diode. In the second and fourth quadrant, the diode generates electric power. In addition, the heat transfer Q between the diode and the emitting body can be evaluated using the formalism as described in Section 2.2.

Depending on the signs of electric power P and the heat flow Q, this system can operate in a wide variety of scenarios. When the diode is facing an emitter with a temperature higher than the diode, the diode can operate in the fourth quadrant and generate electric power from the heat flux into the diode. This is the familiar use of a diode in solar and thermophotovoltaic systems. In this review, we focus on less familiar operation scenarios of the diode in the remaining three quadrants, where the diode can operate either as a solid-state cooler by operating in the first and third quadrant (Section 3), or as a power harvester from outgoing radiation (Section 4).

3. PHOTON-BASED SOLID-STATE COOLING

In the absence of external work input, heat always flows from the hot side to the cold side as required by the second law of thermodynamics.[35] In order to revert the direction of heat flow, one needs to input work to the system. Thus, we consider two different operating regimes of the diode in the first and third quadrants in the I–V plane. When operating in the first quadrant, one places the diode on the cold side and applies a positive voltage bias on the diode [Fig. 4(a)]. The emission from the diode is enhanced over that of a thermal body at the same temperature and hence allows heat to flow from the cold to the hot side.[9,10,27,36–43] When operating in the third quadrant, one places the diode on the hot side and applies a negative voltage bias on the diode [Fig. 4(a)].[32,44–46] The emission from the diode is suppressed below that of a thermal body at the same temperature and hence again allows heat to flow from the cold to the hot side.

The concept of cooling based on a LED has a long history. The first theoretical proposal to achieve cooling by a positively biased LED dates back to the 1950s.[9] However, the experimental progress has been far slower. In 2019, Zhu et al.[46] provided the first experimental demonstration of cooling (i.e., a direct observation of temperature reduction) with a LED operating in the negative bias regime. One of the key advances that led to the

experimental demonstration is the theoretical realization, by Chen et al.,[27,44] that operating in the near field is highly beneficial for demonstrating such solid-state cooling mechanisms. In this section, we provide an overview of the underlying physics of such cooling mechanisms as well as a discussion of the advantage of operating in the near field in overcoming some of nonidealities that are detrimental to the cooling effects in these systems.

3.1 Theoretical Analysis: Ideal Case in the Far Field

In this section, we illustrate the physics of the two cooling mechanisms by considering an ideal diode at a temperature T, emitting through the far field to a blackbody at a temperature T_s. We assume that the diode has unity emissivity above the bandgap and zero emissivity below it. The diode has no nonradiative recombination process. The view factor between the diode and blackbody is assumed to be unity.

We consider the positive-bias case first, where the bias on the diode V and the current injected into the diode I are both positive. The diode is placed on the cold side, i.e., $T < T_s$. Because there is no nonradiative recombination, the current is equal to the net photon flux F emitted by the diode. Hence, the electrical power consumed in the diode is

$$W = qVF \tag{26}$$

where F is given by Eq. (18) with $T_1 = T$ and $T_2 = T_s$. The net cooling power is the difference between the total heat flux and the input electrical power

$$Q_c = Q - W \tag{27}$$

where Q is similarly given by Eq. (13). The coefficient of performance (COP) of the cooler is

$$\text{COP} = \frac{Q_c}{W} \tag{28}$$

Since the emission from the semiconductor is narrow banded, one can estimate the heat flux by

$$Q = \hbar\omega_g F \tag{29}$$

Therefore, the net cooling power is

$$Q_c = (\hbar\omega_g - qV)F \tag{30}$$

Equation (30) can be intuitively understood by noting that each injected electron consumes electrical energy of qV but can carry heat energy of $\hbar\omega_g$ away from the diode through a photon generated from the radiative recombination process. Therefore, the COP can be obtained as follows:

$$\text{COP} = \frac{\hbar\omega_g - qV}{qV} \tag{31}$$

In order to achieve cooling, one must apply a positive voltage on the diode such that $Q_c > 0$. From Eq. (30), this requires $F > 0$ or $f_d(\omega, T, V) > f_s(\omega, T_s, 0)$, which yields[27]

$$V > \frac{\hbar\omega_g}{q}\left(1 - \frac{T}{T_s}\right) \triangleq V_t \tag{32}$$

where V_t is the minimum voltage one must apply in order to achieve cooling. We note that Eq. (32) is in fact exact and can be derived without the narrow-band emission approximation. We refer to V_t as the threshold voltage. When $V = V_t$, the radiant temperature of the diode is equal to the temperature of the hot side

$$T\left(\frac{\hbar\omega_g}{\hbar\omega_g - qV_t}\right) = T_s \tag{33}$$

We now consider the voltage dependence of the cooler. As indicated by Eq. (31), COP reaches the Carnot limit $T/(T_s - T)$ when $V = V_t$, and decreases as V increases when $V > V_t$. The cooling power carried by each emitted photon, $\hbar\omega_g - qV$, also decreases as V increases. However, since the radiation from the diode increases exponentially as the voltage increases, the cooling power Q_c would still increase monotonically as V becomes higher.

When the applied voltage is very close to the bandgap, F is dominated by the emission from the LED. In this case, the cooling power can be approximated as follows:

$$\begin{aligned} Q_{c,\max} &\approx \frac{\omega_g^2}{4\pi^2 c^2} \cdot \frac{C(\omega_g) k_B T}{\hbar} \cdot \frac{\hbar\omega_g - qV}{\exp[(\hbar\omega_g - qV)/k_B T] - 1} \\ &\approx C(\omega_g) \cdot \frac{\omega_g^2}{4\hbar\pi^2 c^2} \cdot (k_B T)^2 \end{aligned} \tag{34}$$

as can be derived from Eq. (30). Here, $C(\omega_g)$ is a dimensionless slowly varying function of ω_g that is typically on the order of unity. For $\hbar\omega_g = 1$ eV, $C(\omega_g) = 1.77$. The maximum cooling power is reached when $qV \to \hbar\omega_g$. Compared to the thermal emission from the same LED in the absence of external bias

$$Q(T, V = 0) \approx \frac{\omega_g^2}{4\pi^2 c^2} \cdot \frac{C(\omega_g) k_B T}{\hbar} \cdot \frac{\hbar\omega_g}{\exp(\hbar\omega_g / k_B T)} \tag{35}$$

We see that the cooling power for the LED is exponentially larger by the factor $(k_B T/\hbar\omega_g)\exp(\hbar\omega_g/k_B T)$. Thus, the cooling power density for such a positively biased LED is not limited by the thermal radiation. In addition, the cooling power density increases quadratically with bandgap. This is in contrast to the thermal emission of an unbiased semiconductor, which decreases exponentially as a function of bandgap size [Eq. (35)]. In this ideal case, there is an advantage of using a large-bandgap semiconductor for cooling applications. We will show that the advantage of using a large-bandgap semiconductor, in fact, is more pronounced in the nonideal case, due in addition to the reduction of the nonradiative Auger recombination as bandgap increases.

To illustrate the cooling performance of such a positively biased LED, in Fig. 5(a) we present an example using an idealized model of a GaAs-based LED with a bandgap energy of 1.44 eV. We assume that the LED is at $T = 3 \times 10^2$ K, and undergoes far-field

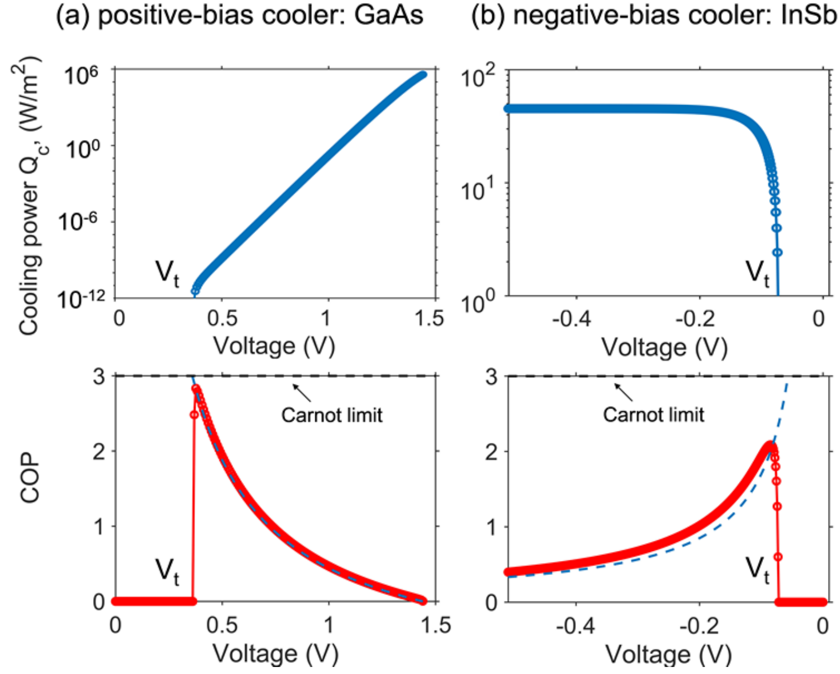

FIG. 5: Cooling power and COP of (a) GaAs-based positive-bias cooler and (b) InSb-based negative-bias cooler in the far field. The temperatures of the hot and cold sides are respectively 4×10^2 and 3×10^2 K. On the COP figures, the black dashed lines are the Carnot limit, and the blue dashed lines are the predictions from Eq. (31) (positive-bias cooler case) and Eq. (39) (negative-bias cooler case).

radiative exchange with a blackbody at a temperature of 4×10^2 K. We achieve a net cooling effect once the applied voltage $V > V_t = 0.36$ V. As V increases beyond V_t, the cooling power Q_c increases near exponentially as a function of V. The COP approaches the Carnot limit of 3 at $V = V_t$ and decreases as V further increases. The calculations here are direct evaluations of Eqs. (26)–(28) without making the narrowband emission approximation. Nevertheless, these numerical results agree very well with the analytic results of Eqs. (29)–(31), indicating that the narrowband emission approximation, in fact, works well for all values of applied voltage considered here.

In Fig. 6(a), we show the numerically computed maximum cooling power as a function of bandgap, under the same condition as above where the LED is maintained at the cold side temperature of 3×10^2 K, facing a blackbody emitter at $T = 4 \times 10^2$ K. The numerical results agree well with Eq. (34), using $C = 1.77$ for all values of ω_g.

Next, we analyze the negative-bias case. Here, we assume a diode on the hot side at a temperature T, undergoing far-field radiative thermal exchange with a blackbody thermal emitter on the cold side at $T_s < T$. The diode is negatively biased, i.e., $V < 0$, and operates in the third quadrant, i.e., $I < 0$. The cooling power is the net radiative heat transfer between the cold side and the hot diode, i.e.,

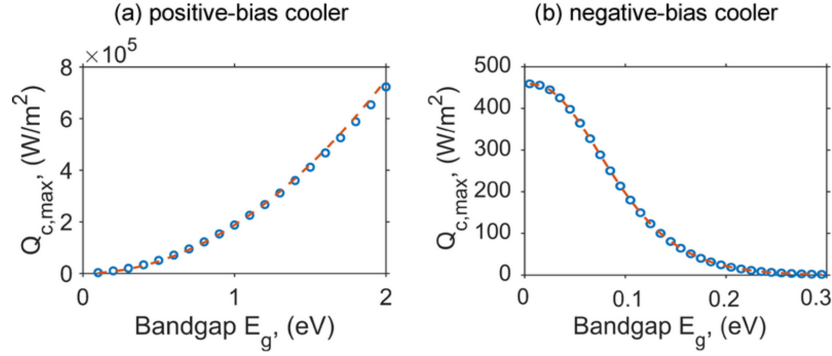

FIG. 6: Maximum cooling power of (a) the positive-bias cooler and (b) negative-bias cooler as a function of the bandgap of the cooler in the far field. The other emitting body is assumed to be a blackbody. The temperatures of the hot side and the cold side are respectively 4×10^2 and 3×10^2 K. In (a), the dashed line is a quadratic fitting based on $Q_{c,\max}$ at 1 eV. In (b), the dashed line is computed based on Eq. (41).

$$Q_c = Q \tag{36}$$

The power consumed in the diode is

$$W = qVF \tag{37}$$

where F is given by Eq. (18) with $T_1 = T$ and $T_2 = T_s$. F is the net above-bandgap photon flux from the hot to the cold side, and the magnitude is equal to the current extracted from the diode from the detailed balance relation of Eq. (24).

Applying the narrowband emission approximation, one can estimate the cooling power as follows:

$$Q_c \approx -\hbar\omega_g F \tag{38}$$

Therefore,

$$\text{COP} = -\frac{\hbar\omega_g}{qV} \tag{39}$$

In order to achieve cooling, we must have $Q_c > 0$, which requires $f_d(\omega, T, V) < f_s(\omega, T_s, 0)$ and leads to[44]

$$V < \frac{\hbar\omega_g}{q}\left(1 - \frac{T}{T_s}\right) \triangleq V_t \tag{40}$$

When V is at the threshold voltage V_t, the radiant temperature of the diode is equal to the temperature of the cold side. Similar to Eq. (32), here Eq. (40) is also exact, and can be derived without the narrowband emission approximation.

From Eq. (40), when $V = V_t$, COP also approaches the Carnot limit $T_s/(T - T_s)$ and then decreases gradually when $V < V_t$. Therefore, the voltage dependence of COP is very similar to that of the positive-bias case.

In contrast to the positive-bias case, as the magnitude of the voltage becomes larger, Q_c increases but gradually saturates. When the magnitude of the applied voltage on the diode is substantial, since the diode is negatively biased, its radiation can be neglected. The cooling power therefore approaches the above bandgap radiative heat flux from the cold side

$$Q_{c,\max} \approx Q_s(T_s, 0) \tag{41}$$

Thus, in the negative-bias case, the maximum cooling power density is limited by the above-bandgap thermal radiation from the cold side and is far lower as compared to that of the positive-bias case. Moreover, since the power density contained in the above-bandgap thermal radiation increases as the bandgap decreases, the negative-bias case favors low-bandgap materials.

To illustrate the discussions above, in Fig. 5(b) we present an example using an idealized InSb diode, which has a bandgap of 0.17 eV. We assume that the diode is at $T = 4 \times 10^2$ K, and undergoes far-field radiative exchange with a blackbody at $T = 3 \times 10^2$ K. The net cooling effect is achieved when the applied voltage $V < V_t = -0.06$ V. The COP drops as the magnitude of the voltage becomes larger, and the predictions from Eq. (39) agree well with the exact calculations.

To illustrate the bandgap dependence of the cooling performance, in Fig. 6(b) we show the maximum cooling power as a function of bandgap, in the same setup as in Fig. 6(a). The maximum cooling power increases monotonically as the bandgap becomes narrower. The predictions of the maximum cooling power from Eq. (41) are plotted in the dashed line, which agrees well with the exact calculations (dots).

Throughout the section, we assume a far-field thermal exchange between the diode and a blackbody emitter. The cooling power density can be further enhanced by operating in the near-field regime.

3.2 Loss Mechanisms in Positive-Bias and Negative-Bias Coolers

In Section 3.1, we focused on the ideal coolers. In practice, the cooling effect is diminished by various loss mechanisms. In general, any heat flows into the object to be cooled, beyond what is required from fundamental thermodynamic considerations, constitutes a loss mechanism. In practice, there are large number of possible loss mechanisms. Here, we review some of the loss mechanisms, including the sub-bandgap absorption of the diode, nonradiative recombination of the diode, and imperfect light extraction from the diode, since these mechanisms are more closely related to underlying optical physics of the diode.

In Section 3.1, we assumed the diode had zero emissivity below the bandgap, and hence there was no sub-bandgap heat transfer. In practice, the diode can have substantial thermal emissivity below bandgap, arising from either free carrier absorption or from the contributions of phonon polaritons, which have been noted to be particularly prominent in near-field configurations.[27] Since the sub-bandgap heat transfer is not regulated by the chemical potential, the direction of the heat flow is always from the hot object to the cold object and, hence, such heat flow represents a parasitic process. Therefore, photon management in the sub-bandgap wavelength region is critical.[27,44,47]

In Section 3.1, we also assumed that the diode had 100% internal quantum efficiency. In other words, every injected electron-photon pair is converted to a photon. In addition to the radiative recombination process, semiconductors also have nonradiative recombination processes, such as the Shockley-Read-Hall (SRH) process or the Auger process. Next, we discuss the impacts of such a nonradiative recombination process for the positive and negative bias coolers separately.

For positive-bias coolers, there is a minimum required value for the external quantum efficiency, defined as the ratio between the outgoing photon flux and the injected electrical current

$$\eta_{\mathrm{EQE}} = \frac{F_d}{I/q} \tag{42}$$

Each injected electron has a probability of η_{EQE} to produce an outgoing photon. From Eq. (30), we see that each outgoing photon results a cooling energy of $\hbar\omega_g - qV$. On the other hand, each electron has a probability of $1-\eta_{\mathrm{EQE}}$ for which it fails to generate an outgoing photon, and instead, it produces a heating energy of qV. A net cooling effect requires the cooling energy exceeds the heating energy, i.e., $\eta_{\mathrm{EQE}}(\hbar\omega_g - qV) > (1-\eta_{\mathrm{EQE}})qV$, which results in the following:[10]

$$\eta_{\mathrm{EQE}} > \frac{qV}{\hbar\omega_g} \tag{43}$$

The above analysis indicates that the requirement for the external quantum efficiency is less stringent when the bias voltage is small. The experiment of Santhanam et al.[38] applied a 70 μV positive bias on a $In_{0.15}Ga_{0.85}As_{0.13}Sb_{0.87}$ infrared LED diode ($E_g = 0.58$ eV). Despite the low external quantum efficiency of the diode ($\eta_{\mathrm{EQE}} \approx 3 \times 10^{-4}$), they observed a 69 pW optical power from a 29.9 pW of input electrical power, which translates to a net cooling power of $\sim$ 39 pW. Taking into account the emitting area of the diode of ~ 8 mm^2, the net cooling power translates to a cooling power density of $\sim$ 4.8 μW/m^2. At such a low cooling power density, they were not able to observe a temperature reduction of the diode.

At low bias, the nonradiative SRH recombination mechanism typically dominates over the radiative recombination. Thus, the internal quantum efficiency at low bias is low. There have been recent efforts seeking to improve the internal quantum efficiency of a diode,[48] which is potentially important for cooling applications. Moreover, as we see in the analysis of the ideal case, to improve power density it is always beneficial to be able to use large bandgap materials such as GaAs and operate at a larger bias voltage.

For a GaAs LED, its internal quantum efficiency increases as a function of voltage until the quasi-Fermi level separation in the diode is approximately $V_0 = 1.14$ V, or about 3×10^2 meV of the bandgap of 1.44 eV.[10] Further increase of voltage beyond V_0 leads to a decrease of the internal quantum efficiency, since the Auger recombination becomes the dominant nonradiative recombination mechanism.[10] On the basis of Eq. (43), at V_0, to achieve cooling requires η_{EQE} of $\sim$ 80%.

The external quantum efficiency can be written as follows:

$$\eta_{\mathrm{EQE}} = \eta_{\mathrm{IQE}} \times \eta_{\mathrm{EXT}} \tag{44}$$

where η_{IQE} and η_{EXT} are the internal quantum efficiency and light extraction efficiency, respectively. The cooling effect therefore requires both η_{IQE} and η_{EXT} to at least exceed 80%. η_{IQE} describes the effect of the nonradiative surface recombination processes and Auger and SRH nonradiative recombination processes.[49] There has been tremendous progress made to improve η_{IQE},[22–24,50–52] and η_{IQE} as high as 99.7% was demonstrated experimentally in a photoluminescent experiment.[22,49] However, the light-extraction efficiency is usually far from the required number because of the index mismatching between the emitting material (refractive index n = 2.5–3.5) and air (refractive index n = 1). For planner emitting surfaces without textures, because of the total internal reflection, only the light within the escape cone can be extracted.[53,54] This puts an upper bound that is about $1/4n^2$ $<$ 10% for η_{EXT}. Therefore, improving η_{EXT} is critical for positive-bias coolers. There have been many proposals to improve light extraction efficiency using nanophotonics approaches.[54] Here, we focus on utilizing the near-field enhancement effect for this purpose.

When two objects are placed within a distance that is smaller than the characteristic wavelength of the radiation in the system, the evanescent waves (the waves outside the light cone) can be efficiently extracted by the photon tunneling effect.[3,27,40,55] Chen et al.[27] first proposed a near-field positive-bias cooler based on InAs diodes. The hot side is a similar polar dielectric (InAs or InSb). The authors showed that even with the nonidealities such as nonradiative recombination process and sub-bandgap heat transfer from phonon polaritons, the system could still achieve net cooling power of $\sim$ 150 W/m^2 with the near-field enhancement effect at a gap spacing of $\sim$ 15 nm, when the hot and cold sides were 3×10^2 and 290 K, respectively. The sub-bandgap parasitic phonon polaritons induced an efficient pathway for heat leakage and therefore substantially reduced the cooling power.

To overcome this, Chen et al.[41] proposed a system based on a GaAs diode. The hot side is Si, which is nonpolar and hence does not support optically active phonon-polaritons. This design strongly suppresses sub-bandgap heat transfer and results in significant improvement in the cooling power and the COP of the system. With a 10 nm gap spacing, the system could achieve a cooling power about 6.96×10^5 W/m^2 when the hot and cold sides are 330 and 280 K, respectively. With the near-field effect, the maximum cooling power can exceed standard thermoelectric coolers even when the nonidealities in the semiconductors and the loss in photon management are considered.[41] Despite these theoretical proposals, experimental demonstrations are still lacking because of the difficulties in maintaining the hot and cold sides in the near field. However, with the advances of the near-field experiment techniques, we expect the positive-bias coolers can be demonstrated in the near future.

We now consider negative-bias coolers. As has been noted in Section 3.1, in contrast to the positive-bias cooler, the negative-bias cooler has a far lower cooling power density. On the other hand, in the negative-bias cooler, the object to be cooled is a passive thermal emitter and is not directly affected by the injection of current to the diode except through radiative heat exchange. Therefore, the requirement for internal quantum efficiency and light extraction for the diode is much less stringent. In practice, a high-efficiency diode is still preferred since the nonidealities can produce a heating power that raises the diode temperature and reduce the cooling power or even cause a net heating effect. Similar to the

positive-bias cooler case, one can also use the near-field enhancement to enhance cooling power.[44] Zhu et al.[46] demonstrated such a near-field enhanced negative-bias cooler. The experimental setup, shown in Fig. 7, consists of an $InAs_{0.7}Sb_{0.3}$ diode with a bandgap of 0.176 eV, separated by a vacuum gap from a calorimeter. The temperature change of the calorimeter can be related to its resistance change. Before the negative bias is applied on the diode, the temperatures of the calorimeter and the diode were ensured to be the same. When a negative bias was applied, by monitoring the resistance change of the calorimeter, the temperature changes of the calorimeter due to cooling (or heating) from the diode could be measured. The measured results are shown in Fig. 8. A cooling effect on the calorimeter is observed when a negative bias is applied on the diode. When the diode is under a negative bias about –0.2 V, the cooling power reaches the maximum value. Further increase of the bias leads to a reduction of the cooling effect due to the temperature increase of the diode caused by the joule heating from the current. Significant enhancement of

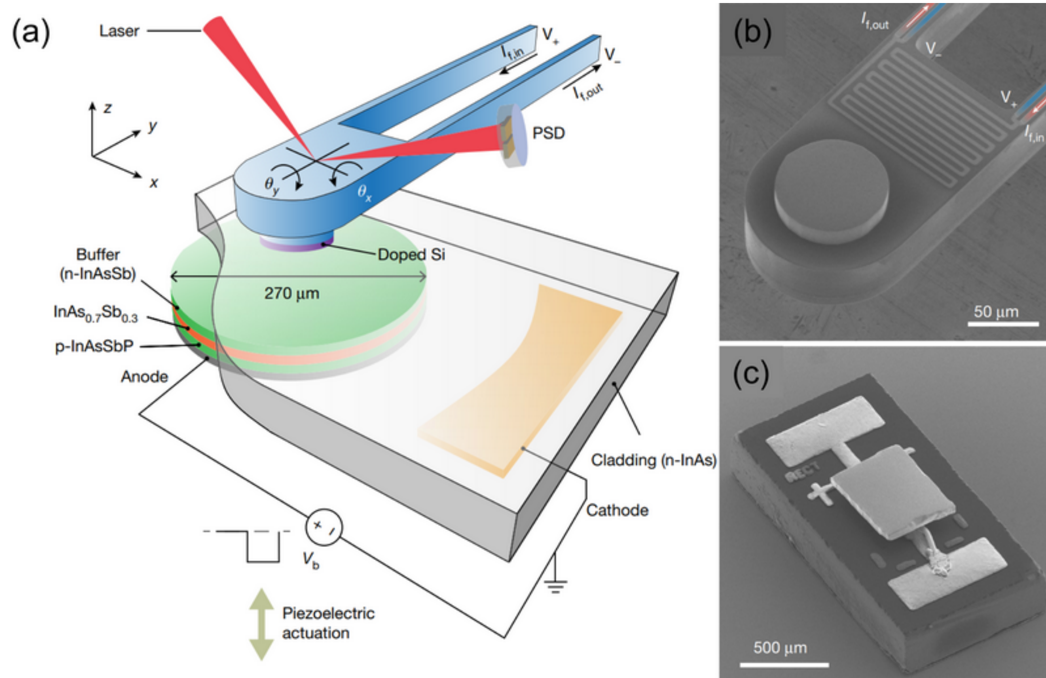

FIG. 7: (a) Schematic of the setup in the experiment by Zhu et al.,[46] consisting of the Doped Si region as the calorimeter, separated from the InAsSb diode by a vacuum gap. The gap size between the calorimeter and photodiode was controlled using a piezoelectric actuator. A position-sensitive detector (PSD) was used to detect contact by monitoring the laser beam reflected from the back of the calorimeter. The thermal resistance network of the calorimeter is also shown. (b) and (c) are the scanning electron microscope images of the custom-designed calorimeter and the photodiode, respectively.[46] (Reprinted with permission from Springer Nature, Copyright 2019)

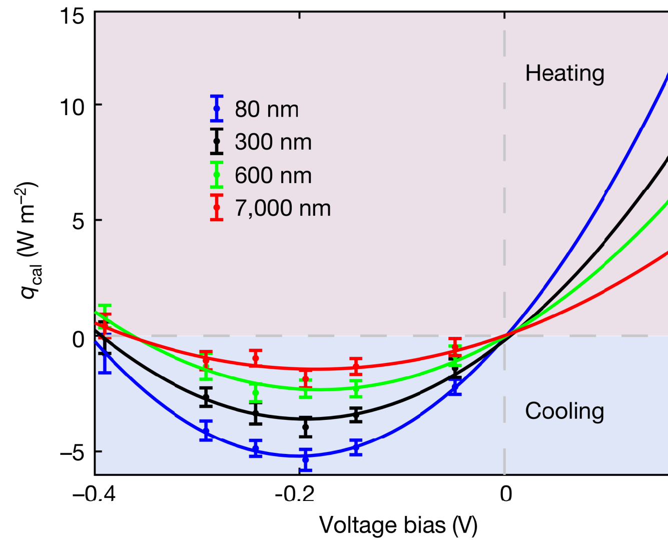

FIG. 8: Measured heat flux to the calorimeter as a function of the voltage bias on the photodiode for various gap sizes by Zhu et al.[46] Solid curves denote quadratic fits.[46] (Reprinted with permission from Springer Nature, Copyright 2019)

the cooling power can be seen in the near-field regime, where the cooling power reaches 6 W/m^2 at gap spacing of 80 nm.

4. POWER GENERATION WITH NONZERO PHOTON CHEMICAL POTENTIAL

In this section, we discuss the power generation based on semiconductor diodes. For power generation purposes, the diode can operate either in the second or the fourth quadrants in the I–V plane (Fig. 4). Photovoltaic power harvesters, such as solar cells and thermophotovoltaic systems, operate in the fourth quadrant. Since photovoltaic power harvesters are well-known, here we focus on negative-illumination power harvester, which operates in the second quadrant. We also discuss the concept of thermophotonics, which combines a positive-bias cooler with a photovoltaic power harvester for power generation.

4.1 Negative-Illumination Power Harvester

Negative-illumination power harvesters are sometimes referred to as thermoradiative cells in the literature.[56–60] In such a power harvester, the diode faces an emitting body with a temperature that is lower than the diode's. As was discussed in Section 2.5, at the open circuit, by detailed balance the diode develops a negative bias. With appropriate load, the diode can operate in the second quadrant for power generation purposes. In contrast to the photovoltaic power harvester, which harvests incoming thermal radiation, a negative-illumination power generates power from outgoing thermal radiation.

In the negative-illumination scenario, the electrical power density produced in the diode is

$$W = -qVF \tag{45}$$

where F, as computed with Eq. (18) with $T_1 = T$ and $T_2 = T_s$, is the net above-bandgap photon flux from the hot diode to the cold surface. The efficiency of the power harvester is

$$\eta = \frac{W}{Q + W} \tag{46}$$

where Q, as computed with Eq. (13), is the net heat flux. For an ideal diode, the highest efficiency occurs near the open circuit situation, where due to the large negative bias, the emission from the diode itself can be neglected. We can thus estimate the maximum efficiency from the following argument. Each electron charge flows through the diode would extract an electric power of $-qV$. Also, the generation of each of such electron corresponds to the emission of a photon from the diode, which carries heat energy of $\hbar\omega$ away from the diode. Therefore, the conversion efficiency can be expressed as follows:[61]

$$\eta = \frac{-qV}{-qV + \hbar\omega} \tag{47}$$

We can obtain the open-circuit voltage by matching the radiant temperature of the diode to that of the colder emitter. As a result

$$V_{oc} = \frac{\hbar\omega_g}{q}\left(1 - \frac{T}{T_s}\right) \tag{48}$$

Therefore, near the open-circuit voltage, the conversion efficiency in Eq. (47) approaches the Carnot efficiency

$$\eta_{\max} = \frac{-qV_{oc}}{-qV_{oc} + \hbar\omega_g} = 1 - \frac{T_s}{T} \tag{49}$$

Similar to a photovoltaic power harvester, the electric power density and the conversion efficiency of a negative-illumination power harvester also depend on the operation point on the I–V curve. In practice, one needs to optimize the load to maximize electrical power density or efficiency.

The maximum power density of a negative illumination power harvester is bandgap-dependent. Since only the above-bandgap photons produce electricity, the power density increases if the diode emits more above-bandgap photons. Therefore, negative illumination power harvesters favor low bandgap diodes. In Fig. 9, we show the maximum power density of a negative-illumination power harvester at 3×10^2 K as a function of the bandgap of the diode. We assume that the diode undergoes a far-field radiative exchange with a 0 K body. The diode has unity emissivity above the bandgap and zero emissivity below the bandgap. The diodes are assumed to be ideal with no nonradiative recombination. The power density increases as the bandgap decreases, reaching the maximum of 54.8 W/m^2

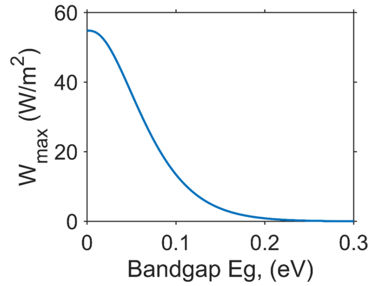

FIG. 9: Maximum power density of a negative-illumination power harvester at 3×10^2 K as a function of the bandgap of the diode in the far field. The emission from the cold surface is neglected.

at the zero-bandgap limit. Therefore, low-bandgap semiconductors are required for this power generation mechanism. The power density can be enhanced beyond the values shown in Fig. 9 by operating in the near field.

In practice, various loss mechanisms, including those mentioned Section 3.2 when discussing the positive- and negative-bias coolers, will also impact the performance of the negative-illumination power harvester. The below-bandgap parasitic heat transfer does not impact the electric power density but does reduce the overall efficiency. The nonradiative recombination loss and light extraction loss reduces both the electric power density and conversion efficiency.

Santhanam and Fan[61] experimentally demonstrated this power generation mechanism. The setup, shown in Fig. 10(a), consists of a HgCdZnTe photodiode facing an infrared-emissive surface, with an optical chopper placed in between to perform lock-in measurement. Both the photodiode and the chopper blade are maintained at a room temperature of 295 K. Figure 10(b) shows the measured photocurrents in two sets of experiments, where the emissive surface was at 305 or 285 K, i.e., either above or below the temperature of the diode. In both experiments, as the chopper rotates, its blade periodically blocks the view of the diode to the emissive surface; thus, the currents vary periodically as a function of time. When the chopper is open, i.e., when the diode can see the emissive surface, from Fig. 4(b) we expect that the direction of the photocurrents is different depending on whether the emissive surface is either hotter or colder than the diode. In the experiment, they indeed observed a 180 deg phase difference in the time variation between the two cases, consistent with the theory for power generation in the negative illumination situation. Figure 10(c) shows the measured power density as a function of the temperature of the emissive surface. The measurement agrees well with the prediction (solid line) based on the above discussions with nonidealities of the diode included.

Ono et al.[62] applied the same principle to directly harvest energy from the cold universe by having a diode facing the sky. An image of the experimental setup is shown in Fig. 11(a). The atmosphere is transparent in the wavelength range of 8–13 μm. Ono et al. chose a diode with a cutoff wavelength of 8.27 μm at room temperature so that part of the above-bandgap emission of the diode passes through the atmosphere. The radiation

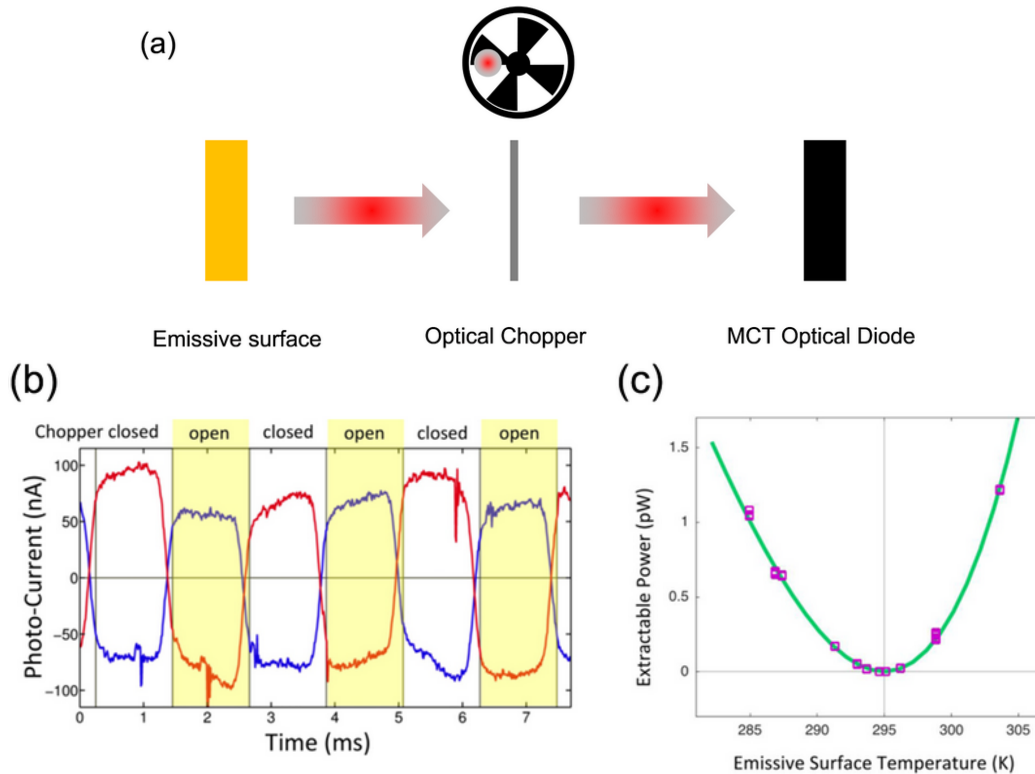

FIG. 10: (a) Schematic of the experimental setup used by Santhanam and Fan.[61] An emissive surface faces an MCT optical diode, with an optical chopper placed in the middle of the radiation pathway for lock-in measurement. (b) Photocurrents as a function of time, red and blue correspond to the cases with either high (305 K) or low (285 K) emissive surface temperatures, respectively. (c) Extractable power versus temperature of the emissive surface facing the diode; the discrete points are the experiment results. The solid line represents a model, including nonidealities of the diode.[61] (Reprinted with permission from the American Physical Society, Copyright 2016)

from the diode is redirected by a parabolic mirror to the sky. A similar lock-in technique to Santhanam and Fan[61] was used to obtain the photocurrent. When the diode is at room temperature (297 K), the measured electrical power is 6.39×10^{-2} μW/m^2, as shown in Fig. 11(b). There is significant potential to further improve the power density by using diodes with lower nonradiative recombination and by improving the spectral overlap of the diode emission with the transparency window of the atmosphere.

4.2 Thermophotonic System for Power Generation

In Sections 3.1–4.1, we consider systems with only one diode. It is in fact possible to consider systems with multiple diodes operating in different quadrants, undergoing radiative

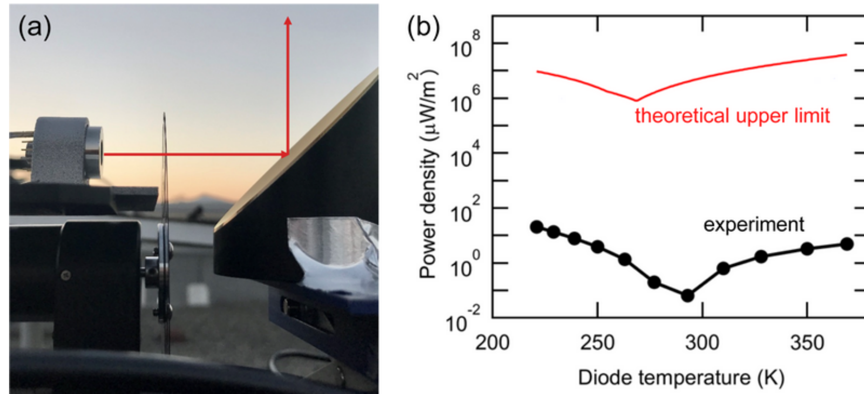

FIG. 11: (a) Experimental setup used by Ono et al.[62] The image shows the diode, the chopper blade, and the parabolic mirror to redirect the radiation from the diode to the sky. The pathway of radiation is illustrated with the dashed lines. (b) Calculated power density as a function of the diode temperature with the experimental condition (black-dotted curve); the upper limit of the power densities calculated by the detailed-balance model is shown by the red curve (assuming perfect external quantum efficiency but taking into account the emissivity of the atmosphere).[62] (Reprinted with permission from AIP Publishing, Copyright 2019)

exchange among them. Such systems could yield higher power density for power harvesters or better coefficient of performance for coolers. Here we focus on thermophotonic system, which consists of a positive-bias cooler and a photovoltaic power harvester. We discuss the working principle of the system and present a circuit that makes the system self-sustaining.

4.2.1 Thermophotonic System

The concept of a thermophotonic system was introduced by Green over 20 years ago.[63] This system,[8] as shown in Fig. 12, consists of a LED on the hot side and a photovoltaic (PV) cell on the cold side. The LED operates as a positive-bias cooler, and the PV cell as a photovoltaic energy harvester. The LED converts input heat to a photon. The emitted photon from the LED is absorbed by the PV cell to produce electricity [Fig. 12(a)]. Compared to the standard thermophotovoltaic system [Fig. 12(b)],[64–76] which uses a passive thermal emitter on the hot side, a thermophotonic system can achieve much higher power density because of the power density enhancement in the positive-bias cooler, as discussed in Section 3.1.[77–80]

Next we conduct an analysis in order to highlight the underlying physics of the thermophotonic system. We assume both the LED and the PV cell are ideal with no nonradiative recombination. The view factor between them is unity. They have the same bandgap energy. Both the LED and the PV cell have unity emissivity above the bandgap and zero emissivity below. On the basis of the detailed balance relation in Eq. (24), we can obtain

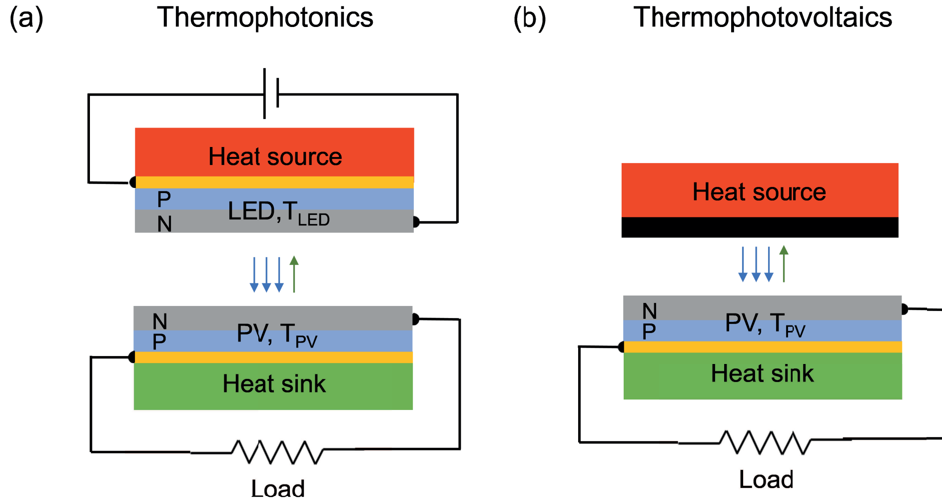

FIG. 12: (a) Schematic of a thermophotonic system using batteries. The battery connected to the LED is used to drive the LED. (b) Schematic of a thermophotovoltaic system.

equations for the currents I_{LED} and I_{PV} and the voltages V_{LED} and V_{PV}, for the LED and the PV cell, as follows:

$$F_{\text{PV-LED}} - F_{\text{LED-PV}} + \frac{I_{\text{LED}}}{q} = 0 \tag{50}$$

and

$$F_{\text{LED-PV}} - F_{\text{PV-LED}} + \frac{I_{\text{PV}}}{q} = 0 \tag{51}$$

In Eqs. (50) and (51), $F_{a\text{-}b}$ is the photon flux emitted by object a and received by object b, where a, b = PV and LED. From these equations, we see that $I_{\text{LED}} = -I_{\text{PV}} \equiv I$. To apply positive bias on the LED, in principle one can assume that the LED is driven by an external battery, as shown in Fig. 12. In most theoretical analyses of thermophotonic systems, one further assumes that the battery can somehow be recharged using the electricity produced in the PV cell.[8,78,81] The net output power of a thermophotonic system is then[79]

$$W = I(V_{\text{PV}} - V_{\text{LED}}) \tag{52}$$

The heat flow extracted from the heat source is

$$Q = Q_{\text{LED}}(T_{\text{LED}}, V_{\text{LED}}) - Q_{\text{PV}}(T_{\text{PV}}, V_{\text{PV}}) - I_{\text{LED}}V_{\text{LED}} \tag{53}$$

Therefore, the efficiency of the system is

$$\eta = \frac{W}{Q} \tag{54}$$

Equation (52) indicates that the power density of the thermophonic system is dependent on the voltages on the LED (V_{LED}) and the PV cell (V_{PV}). V_{LED} can be controlled externally. V_{PV} can be controlled through the choice of the external load. The maximum power point and the maximum efficiency point of the system can be identified by searching the parameter space of V_{LED} and the external load. In Fig. 13, we plot as circles the maximum power density (W_{max}) as a function of the bandgap, as obtained from such a search. We assume the temperatures $T_{\text{PV}} = 3 \times 10^2$ and $T_{\text{LED}} = 6 \times 10^2$ K. We note that the power density of heat transfer between two planar blackbodies at temperatures 6×10^2 and 3×10^2 K is approximately 6.9×10^3 W/m^2. The extracted electric power in the thermophotonic system can far exceed such a blackbody limit even in the far-field regime, and further enhancement of power density can be achieved by operating in the near field.

In obtaining the results of Fig. 13, we observe that the maximum power density occurs when both V_{LED} and V_{PV} are close to the bandgap voltage $V_g \equiv \hbar\omega_g/q$. And moreover, the maximum power density shows a quadratic dependence on ω_g, as shown by the solid line in Fig. 13. These observations can be understood as follows. The LED has a high power density when the bias V_{LED} is close to the bandgap voltage $V_g \equiv \hbar\omega_g/q$. Thus, it is reasonable to expect that the thermophotonics system also has a high power density when $V_{\text{LED}} \approx V_g$. Moreover, in order to ensure the system has a net positive power generation, from Eq. (52) we need to have $V_{\text{PV}} > V_{\text{LED}}$. Therefore, at the maximum power point, we should have $V_{\text{PV}} \approx V_g$ as well. In this case, we can apply the same analysis leading to Eq. (34) and obtain

$$F_{\text{LED-PV}} \approx \frac{\omega_g^2}{4\pi^2 c^2} \frac{C(\omega_g) k_B T_{\text{LED}}}{\hbar} \frac{1}{\exp[(\hbar\omega_g - qV_{\text{LED}})/k_B T_{\text{LED}}] - 1} \tag{55}$$

and

$$F_{\text{PV-LED}} \approx \frac{\omega_g^2}{4\pi^2 c^2} \frac{C(\omega_g) k_B T_{\text{PV}}}{\hbar} \frac{1}{\exp[(\hbar\omega_g - qV_{\text{PV}})/k_B T_{\text{PV}}] - 1} \tag{56}$$

Therefore, near the maximum power point, we can approximate the power density as follows:

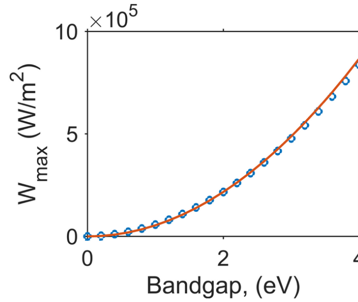

FIG. 13: Maximum power density of the thermophonic system in the far field when the temperatures of the hot and cold sides are respectively 6×10^2 and 3×10^2 K. The solid line is a fit with a quadratic function.

$$W \approx C(\omega_g)\frac{qk_B\omega_g^2}{4\hbar\pi^2c^2} \times \left\{\frac{T_{\text{LED}}(V_{\text{PV}}-V_{\text{LED}})}{\exp\left[(\hbar\omega_g-qV_{\text{LED}})/k_BT_{\text{LED}}\right]-1}-\frac{T_{\text{PV}}(V_{\text{PV}}-V_{\text{LED}})}{\exp\left[(\hbar\omega_g-qV_{\text{PV}})/k_BT_{\text{PV}}\right]-1}\right\} \quad (57)$$

Since V_{LED} and V_{PV} are both close to V_g near the maximum power point, the PV cell operating status is quite close to the open circuit condition, i.e., the load in Fig. 12(a) is quite large. In this scenario, the radiant temperatures of the LED and the PV are quite close. On the basis of Eq. (23), we have

$$\frac{T_{\text{LED}}}{\hbar\omega_g-qV_{\text{LED}}} \approx \frac{T_{\text{PV}}}{\hbar\omega_g-qV_{\text{PV}}} \quad (58)$$

Using Eq. (58), Eq. (57) can be written as follows:

$$\begin{aligned} W &\approx \frac{C(\omega_g)\,\omega_g^2}{4\hbar\pi^2c^2}k_B\left(T_{\text{LED}}-T_{\text{PV}}\right) \\ &\times \left\{\frac{\hbar\omega_g-qV_{\text{LED}}}{\exp\left[(\hbar\omega_{\text{g}}-qV_{\text{LED}})/k_BT_{\text{LED}}\right]-1}-\frac{\hbar\omega_g-qV_{\text{PV}}}{\exp\left[(\hbar\omega_g-qV_{\text{PV}})/k_BT_{\text{PV}}\right]-1}\right\} \\ &\approx \frac{C(\omega_g)\,\omega_g^2}{4\hbar\pi^2c^2}\left[k_B\left(T_{\text{LED}}-T_{\text{PV}}\right)\right]^2 \end{aligned} \quad (59)$$

which is quite similar to the formula for the maximum cooling power shown as Eq. (34). Since the term in the bracket is independent on the bandgap, the maximum power density therefore scales as ω_g^2 (Fig. 13).

Since in the thermophotonic system the LED operates as a positive-bias cooler, thermophonic systems have the same set of requirements regarding the need to suppress various loss mechanisms as the positive-bias cooler, as discussed in Section 3.2. Similar to the positive-bias cooler, operating in the near-field can be beneficial not only for power density enhancement but also for reducing the impacts of various loss mechanisms. Zhao et al.[79] proposed a near-field thermophotonic system that can operate despite the existence of the loss mechanisms (Fig. 14). The temperatures of the PV cell and the LED are chosen 3×10^2 and 6×10^2 K, respectively, in order to demonstrate the potential application of thermophotonic systems for the recovery of low-grade waste heat. The proposed thermophotonic system was based on the $\text{Al}_x\text{Ga}_{1-x}\text{As}$ material system, as shown in Fig. 14(a). The LED has $x = 0.32$, and the PV cell has $x = 0.155$. These material choices ensure that the bandgaps of the LED and the PV cell align even though their temperatures differ. The performance of the system as a function of the voltage on the LED V_{LED} is shown in Fig. 14(b). For each fixed V_{LED}, the curves show the optimized efficiency or power density as one varies the output voltage V_{PV} from the PV cell. In the far-field case where $d = 1$ μm, when V_{LED} is zero, the LED is a passive thermal emitter and the system operates as a thermophotovoltaic system. In this case, the thermal radiation from the LED that is above the bandgap of the PV cell (1.64 eV) is 0.006 pW/m^2. Thus, the output power density is

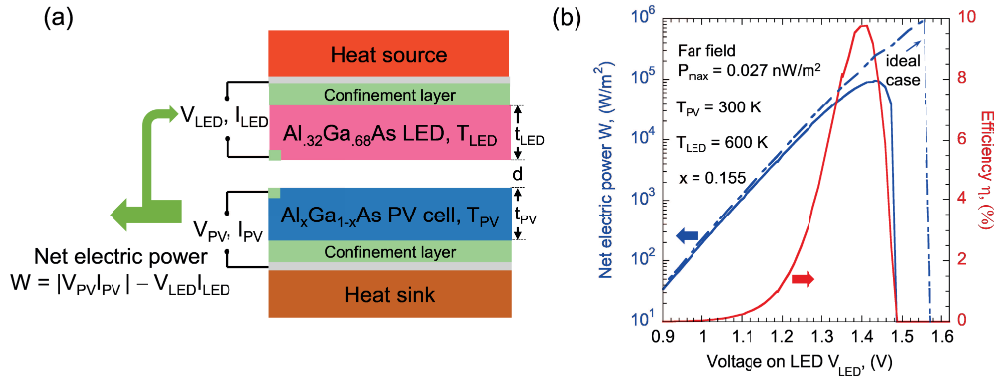

FIG. 14: (a) Schematic of a proposed thermophotonic system for waste heat recovery. The thicknesses of the cell and the LED are t_{PV} and t_{LED}, respectively, and the gap spacing between the LED and the PV cell is denoted by d. The forward biases on the cell and LED are V_{PV} and V_{LED}, respectively, while the current densities are I_{PV} and I_{LED}, respectively. Both the LED and cell have Ag back mirrors (thick silvery lines) of photon recycling. These back mirrors also serve as metal contacts. The active regions of the LED and PV cell are separated from the metal contacts by Al.8Ga.2As carrier confinement layers (5×10^2 nm thick). (b) The net power and conversion efficiency of the proposed system as a function of the bias on the LED. The curves are computed with $d = 10$ nm. The power and efficiency curves are calculated with all the realistic nonidealities of the system. t_{PV} and t_{LED} are set to be 9×10^2 nm. In obtaining the power curve for the ideal case, it is assumed that the LED and the PV cell are infinitely thick, the photons are perfectly recycled, and the nonradiative recombination rate is zero.[79] (Reprinted with permission from the American Chemical Society, Copyright 2018)

negligibly small. The output power density can be significantly improved to 0.027 nW/m^2 at $V_{\mathrm{LED}} = 0.63$ V, which is about five orders of magnitude larger compared to the scenario when the LED is not biased. We note that theoretically the maximum power density can reach 1.48×10^5 W/m^2, based on Fig. 13, if the diodes are free of nonidealities, such as nonradiative loss and light extraction loss. This highlights the importance of high-quality optoelectronic devices in thermophotonic systems, especially for far-field thermophotonic systems.

When d is decreased to 10 nm, the system operates in the near-field regime. At a higher bias voltage, $V_{\mathrm{LED}} = 1.43$ V, the maximum power density increases to 9.58×10^4 W/m^2, as shown in the solid curve. At this maximum power point, the voltage of the PV cell is $V_{\mathrm{PV}} = 1.52$ V. At the maximum power point, the corresponding efficiency η is 8.47%. The efficiency of the system, which is obtained for a fixed V_{LED} by maximizing the efficiency with respect to V_{PV}, also follows a similar trend as shown in the solid curve. The maximum efficiency, η is 9.76%, is reached at a lower voltage when $V_{\mathrm{LED}} = 1.41$ V. We note that with the near-field enhancement effect, even after considering all the nonidealities in the thermophotonic system, the maximum power density and the efficiency can

outperform state-of-the-art thermoelectric generators.[82] This highlights the importance of the near-field enhancement to thermophotonic systems. In the ideal case, assuming zero nonradiative recombination rates and perfect back mirrors, the system can yield a power density of 9.7×10^5 W/m^2, indicating that further improvements are possible.

We note that for a thermophotonic system, one need not choose a narrowband semiconductor even when the purpose is to recover low-grade heat. This is in contrast to the photovoltaic power harvesters, where a PV cell using a narrowband semiconductor is required when the temperature of the heat source is low. Using a larger bandgap semiconductor for these energy applications is a significant advantage since nonradiative recombination, especially, the Auger recombination, is significantly weaker in larger bandgap semiconductors. Here, the AlGaAs system is chosen for its relatively low nonradiative recombination rate. Alternatively, one may consider using nonpolar semiconductors such as Si and Ge for the PV cell, to eliminate the phonon-polariton effects that contribute to sub-bandgap heat transfer,[47] or using GaN-based material system if a higher operating temperature is desired.

The thermophotonic concept can also be used in positive-bias cooling systems to further improve their performance. Chen et al.[41] consider a system with a GaAs LED on the cold side. The LED is subject to a positive bias to achieve cooling. Unlike the system considered Section 3, here the hot side a Si PV cell. The PV cell converts part of the emission from the LED into electric power. The overall system therefore has lower net power consumption and a higher COP, as compared to a system where the hot side is a conventional thermal emitter.[10]

4.2.2 Self-Sustaining Thermophotonic Circuit

As discussed in Section 4.2.1, in thermophotonic system the LED on the hot side needs to be biased. To apply this positive bias on the LED, at least in principle, one can assume that the LED is driven by an external battery as shown in Fig. 12. In most theoretical analyses of thermophotonic systems, including the discussion in Section 4.2.1, one further assumes that the battery can somehow be recharged using the electricity produced in the PV cell.[8,78,81] The net output of a thermophotonic system is then computed by taking the output power of the PV cell minus the power that is required to charge the battery, as we have done in Section 4.2.1.[79] It would be far more attractive if one can design a circuit such that part of the electricity produced by the PV cell can be used to directly provide the positive bias on the LED, i.e., to make the system self-sustaining. In this section, we review the recent work of Zhao et al.,[83] which introduced such a self-sustaining circuit.

To understand some of the difficulties associated with constructing such a self-sustaining circuit, we first consider a simple thermophotonic circuit with one LED and one PV cell as shown in Fig. 15(a), where a resistor R is used in the circuit as a load. This geometry is the same as in Fig. 12, except we now directly connect the LED and the PV cell. We again assume ideal LED and PV cell. In order to operate this system as a thermophotonic circuit for the purpose of thermal energy harvesting, we assume $T_{\mathrm{LED}} > T_{\mathrm{PV}}$.

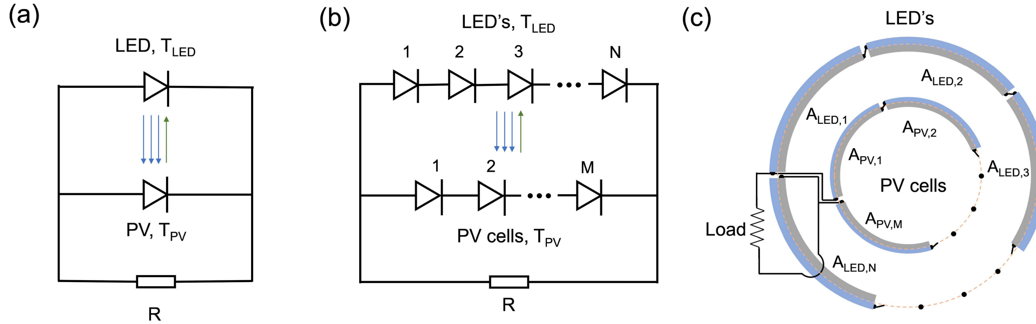

FIG. 15: (a) Circuit where a resistor is connected in parallel with the PV cell and the LED. The load is represented by a resistor with a resistance R. (b) Proposed thermophotonic circuit that uses multiple LEDs (N in total) and multiple PV cells (M in total) by Zhao et al.[83] It is assumed that $N > M$. The load is a resistor with a resistance R. (c) Schematic of the physical connections of the LEDs, PV cells, and the load, with the LEDs and the PV cells arranged in the symmetric configuration. The areas of each PV cell and LED are $A_{\mathrm{PV},i}$, and $A_{\mathrm{LED},j}$, respectively, with $i = 1, 2, ..., M$, and $j = 1, 2, ..., N$.[83] (Adapted from Zhao et al.)

For the circuit as shown in Fig. 15(a), Eqs. (50) and (51) show that the magnitudes of the currents in the PV cell and the LED are the same. Therefore, the current passing through the load must be zero and the voltages on the PV cell and the LED are both zero. In fact, the voltages are zero in the circuit even when the PV cells and the LEDs possess the nonradiative processes.[83] One can intuitively understand this since each electron produced by the PV cell must at least consume one photon emitted by the LED. And, each injected electron into the LED at most can produce one photon. Therefore, no excess electrons can be produced to drive the load.

On the basis of the analysis of the simple circuit above, then the key intuition toward creating a self-sustaining circuit is to decouple the number of injected electrons to the LED and the number of photons generated. From this intuition, Zhao et al.[83] proposed a circuit as shown in Fig. 15(b). Compare to the geometry in Fig. 15(a), in this system the hot side has $N > 1$ number of LEDs connected in series, and the cold side has $M \geq 1$ number of PV cells connected in series. Each electron passing through the LEDs can produce multiple photons and therefore allows a nonzero current to drive the load. Figure 15(c) shows a more detailed physical configuration for this kind of circuit. Here, all LEDs are the same and so are all PV cells. The LEDs and the PV cells are assumed to have the same bandgap at their respective temperatures. The LEDs and the PV cells are arranged in a symmetric configuration. By symmetry then, one can show that when $N > M$, the photon flux injected into a PV cell, $A_{\mathrm{PV}}[F_{\mathrm{LED}}(T_{\mathrm{LED}}, V_{\mathrm{LED}}) - F_{\mathrm{PV}}(T_{\mathrm{PV}}, V_{\mathrm{PV}})]$, exceeds the electron flux injected into the LEDs, $M/N A_{\mathrm{PV}}[F_{\mathrm{LED}}(T_{\mathrm{LED}}, V_{\mathrm{LED}}) - F_{\mathrm{PV}}(T_{\mathrm{PV}}, V_{\mathrm{PV}})]$, where A_{PV} is the area of a PV cell. Thus, part of the current generated by the PV cell can be used to drive

the external load and make the system self-sustaining. The self-sustaining thermophotonic circuit proposed by Zhao et al.[83] can be important for a number of applications, such as solar energy harvesting[77] and waste heat recovery.[79] The realization that the electron and photon flux need not be strictly equal even in ideal systems in this design may also point to previously unexplored flexibilities in designing optoelectronic devices for energy applications.

5. CONCLUSIONS

In this chapter, we review the use of the concepts of the chemical potential of photons, as exhibited in semiconductor photodiode under external bias, for radiative heat transfer control and power generation. We show that the understanding of this concept leads to novel opportunities beyond the traditional solar cells and thermophotovoltaic systems. These opportunities include electroluminescent cooling, power generation from negative illumination, and thermophotonic circuits for power generation where the performance can far exceed traditional thermophotovoltaic systems. The near-field enhancement effect can be applied to all of the abovementioned scenarios and enhance the performance of the system. We believe that, with the advance of the near-field technologies and the continuous improvement of the semiconductors, the concept of photon chemical potential can enable even more exciting opportunities in heat transfer and energy applications.

ACKNOWLEDGMENT

The authors acknowledge the support of the Department of Energy "Photonics at Thermodynamic Limits" Energy Frontier Research Center under Grant No. DESC0019140.

REFERENCES

1. Wurfel, P., The Chemical Potential of Radiation, *J. Phys. C*, vol. **15**, p. 3967, 1982.
2. Planck, M., *The Theory of Heat Radiation*, London: Forgotten Books, 2013.
3. Zhang, Z.M., *Nano/Microscale Heat Transfer*, New York: McGraw-Hill, 2007.
4. Shockley, W. and Queisser, H.J., Detailed Balance Limit of Efficiency of P-N Junction Solar Cells, *J. Appl. Phys*., vol. **32**, pp. 510–519, 1961.
5. Kittel, C. and Kroemer, H., *Thermal Physics*, New York: W.H. Freeman and Company, 1980.
6. Landsberg, P.T., Photons at Non-Zero Chemical Potential, *J. Phys. C*, vol. **14**, pp. L1025–L1027, 1981.
7. Ries, H. and McEvoy, A.J., Chemical Potential and Temperature of Light, *J. Photochem. Photobiol. A*, vol. **59**, pp. 11–18, 1991.
8. Green, M.A., *Third Generation Photovoltaics: Advanced Solar Energy Conversion*, New York: Springer, 2006.
9. Tauc, J., The Share of Thermal Energy Taken from the Surroundings in the Electro-Luminescent Energy Radiated from a P-N Junction, *Czech. J. Phys*., vol. **7**, pp. 275–276, 1957.

10. Xiao, T.P., Chen, K., Santhanam, P., Fan, S., and Yablonovitch, E., Electroluminescent Refrigeration by Ultra-Efficient GaAs Light-Emitting Diodes, *J. Appl. Phys.*, vol. **123**, p. 173104, 2018.
11. Rousseau, E., Siria, A., Jourdan, G., Volz, S., Comin, F., Chevrier, J., and Greffet, J.-J., Radiative Heat Transfer at the Nanoscale, *Nat. Photonics*, vol. **3**, pp. 514–517, 2009.
12. Shen, S., Narayanaswamy, A., and Chen, G., Surface Phonon Polaritons Mediated Energy Transfer between Nanoscale Gaps, *Nano Lett.*, vol. **9**, pp. 2909–2913, 2009.
13. Guha, B., Otey, C., Poitras, C.B., Fan, S., and Lipson, M., Near-Field Radiative Cooling of Nanostructures, *Nano Lett*., vol. **12**, pp. 4546–4550, 2012.
14. Song, B., Ganjeh, Y., Sadat, S., Thompson, D., Fiorino, A., Fernandez-Hurtado, V., Feist, J., Garcia-Vidal, F.J., Cuevas, J.C., Reddy, P., and Meyhofer, E., Enhancement of Near-Field Radiative Heat Transfer Using Polar Dielectric Thin Films, *Nat. Nanotechnol*., vol. **10**, pp. 253–258, 2015.
15. Watjen, J.I., Zhao, B., and Zhang, Z.M., Near-Field Radiative Heat Transfer between Doped-Si Parallel Plates Separated by a Spacing Down to 200 nm, *Appl. Phys. Lett*., vol. **109**, p. 203112, 2016.
16. St-Gelais, R., Zhu, L., Fan, S., and Lipson, M., Near-Field Radiative Heat Transfer between Parallel Structures in the Deep Subwavelength Regime, *Nat. Nanotechnol.*, vol. **11**, pp. 515–519, 2016.
17. Ghashami, M., Geng, H., Kim, T., Iacopino, N., Cho, S.K., and Park, K., Precision Measurement of Phonon-Polaritonic Near-Field Energy Transfer between Macroscale Planar Structures under Large Thermal Gradients, *Phys. Rev. Lett*., vol. **120**, p. 175901, 2018.
18. Yang, J., Du, W., Su, Y., Fu, Y., Gong, S., He, S., and Ma, Y., Observing of the Super-Planckian Near-Field Thermal Radiation between Graphene Sheets, *Nat. Commun.*, vol. **9**, p. 4033, 2018.
19. Inoue, T., Koyama, T., Kang, D.D., Ikeda, K., Asano, T., and Noda, S., One-Chip Near-Field Thermophotovoltaic Device Integrating a Thin-Film Thermal Emitter and Photovoltaic Cell, *Nano Lett*., vol. **19**, pp. 3948–3952, 2019.
20. DeSutter, J., Tang, L., and Francoeur, M., A Near-Field Radiative Heat Transfer Device, *Nat. Nanotechnol*., vol. **14**, pp. 751–755, 2019.
21. Thomas, N.H., Sherrott, M.C., Broulliet, J., Atwater, H.A., and Minnich, A.J., Electronic Modulation of Near-Field Radiative Transfer in Graphene Field Effect Heterostructures, *Nano Lett*., vol. **19**, pp. 3898–3904, 2019.
22. Schnitzer, I., Yablonovitch, E., Caneau, C., and Gmitter, T.J., Ultrahigh Spontaneous Emission Quantum Efficiency, 99.7% Internally and 72% Externally, from AlGaAs/GaAs/AlGaAs Double Heterostructures, *Appl. Phys. Lett*., vol. **62**, pp. 131–133, 1993.
23. Gardner, N.F., Müller, G.O., Shen, Y.C., Chen, G., Watanabe, S., Götz, W., and Krames, M.R., Blue-Emitting InGaN–GaN Double-Heterostructure Light-Emitting Diodes Reaching Maximum Quantum Efficiency above 200 A/cm^2, *Appl. Phys. Lett*., vol. **91**, p. 243506, 2007.
24. Piprek, J., Blue Light Emitting Diode Exceeding 100% Quantum Efficiency, *Phys. Status Solidi RRL*, vol. **8**, pp. 424–426, 2014.
25. Hurni, C.A., David, A., Cich, M.J., Aldaz, R.I., Ellis, B., Huang, K., Tyagi, A., DeLille, R.A., Craven, M.D., Steranka, F.M., and Krames, M.R., Bulk Gan Flip-Chip Violet Light-Emitting Diodes with Optimized Efficiency for High-Power Operation, *Appl. Phys. Lett*., vol. **106**, p. 031101, 2015.

26. Callen, H.B. and Welton, T.A., Irreversibility and Generalized Noise, *Phys. Rev.*, vol. **83**, pp. 34–40, 1951.
27. Chen, K., Santhanam, P., Sandhu, S., Zhu, L., and Fan, S., Heat-Flux Control and Solid-State Cooling by Regulating Chemical Potential of Photons in Near-Field Electromagnetic Heat Transfer, *Phys. Rev. B*, vol. **91**, p. 134301, 2015.
28. Joulain, K., Mulet, J.-P., Marquier, F., Carminati, R., and Greffet, J.-J., Surface Electromagnetic Waves Thermally Excited: Radiative Heat Transfer, Coherence Properties and Casimir Forces Revisited in the Near Field, *Surf. Sci. Rep.*, vol. **57**, pp. 59–112, 2005.
29. Basu, S., Zhang, Z.M., and Fu, C.J., Review of Near-Field Thermal Radiation and Its Application to Energy Conversion, *Int. J. Energy Res.*, vol. **33**, pp. 1203–1232, 2009.
30. Jones, A.C., O'Callahan, B.T., Yang, H.U., and Raschke, M.B., The Thermal Near-Field: Coherence, Spectroscopy, Heat-Transfer, and Optical Forces, *Prog. Surf. Sci.*, vol. **88**, pp. 349–392, 2013.
31. Song, B., Fiorino, A., Meyhofer, E., and Reddy, P., Near-Field Radiative Thermal Transport: From Theory to Experiment, *AIP Adv*., vol. **5**, p. 053503, 2015.
32. Berdahl, P., Radiant Refrigeration by Semiconductor Diodes, *J. Appl. Phys*., vol. **58**, pp. 1369–1374, 1985.
33. Pankove, J.I., *Optical Processes in Semiconductors*, New York: Doover Publications, 1971.
34. Schubert, E.F., *Light-Emitting Diodes*, Cambridge, UK: Cambridge University Press, 2006.
35. Bergman, T.L., Lavine, A.S., Incropera, F.P., and DeWitt, D.P., *Fundamentals of Heat and Mass Transfer*, Hoboken, NJ: Wiley, 2017.
36. Dousmanis, G.C., Mueller, C.W., Nelson, H., and Petzinger, K.G., Evidence of Refrigerating Action by Means of Photon Emission in Semiconductor Diodes, *Phys. Rev*., vol. **133**, pp. A316–A318, 1964.
37. Oksanen, J. and Tulkki, J., Thermophotonic Heat Pump—A Theoretical Model and Numerical Simulations, *J. Appl. Phys.*, vol. **107**, p. 093106, 2010.
38. Santhanam, P., Gray, D.J., and Ram, R.J., Thermoelectrically Pumped Light-Emitting Diodes Operating above Unity Efficiency, *Phys. Rev. Lett*., vol. **108**, p. 097403, 2012.
39. Santhanam, P., Huang, D., Ram, R.J., Remennyi, M.A., and Matveev, B.A., Room Temperature Thermo-Electric Pumping in Mid-Infrared Light-Emitting Diodes, *Appl. Phys. Lett*., vol. **103**, p. 183513, 2013.
40. Liu, X. and Zhang, Z.M., High-Performance Electroluminescent Refrigeration Enabled by Photon Tunneling, *Nano Energy*, vol. **26**, pp. 353–359, 2016.
41. Chen, K., Xiao, T.P., Santhanam, P., Yablonovitch, E., and Fan, S., High-Performance Near-Field Electroluminescent Refrigeration Device Consisting of a GaAs Light Emitting Diode and a Si Photovoltaic Cell, *J. Appl. Phys.*, vol. **122**, p. 143104, 2017.
42. Sadi, T., Kivisaari, P., Tiira, J., Radevici, I., Haggren, T., and Oksanen, J., Electroluminescent Cooling in Intracavity Light Emitters: Modeling and Experiments, *Opt. Quant. Electron*., vol. **50**, p. 18, 2017.
43. Liao, T., Tao, C., Chen, X., and Chen, J., Parametric Optimum Design of a Near-Field Electro-Luminescent Refrigerator, *J. Phys. D*, vol. **52**, p. 325108, 2019.
44. Chen, K., Santhanam, P., and Fan, S., Near-Field Enhanced Negative Luminescent Refrigeration, *Phys. Rev. Appl*., vol. **6**, p. 024014, 2016.

45. Lin, C., Wang, B., Teo, K., and Zhang, Z., A Coherent Description of Thermal Radiative Devices and Its Application on the Near-Field Negative Electroluminescent Cooling, *Energy*, vol. **147**, pp. 177–186, 2018.
46. Zhu, L., Fiorino, A., Thompson, D., Mittapally, R., Meyhofer, E., and Reddy, P., Near-Field Photonic Cooling through Control of the Chemical Potential of Photons, *Nature*, vol. **566**, pp. 239–244, 2019.
47. Chen, K., Santhanam, P., and Fan, S., Suppressing Sub-Bandgap Phonon-Polariton Heat Transfer in Near-Field Thermophotovoltaic Devices for Waste Heat Recovery, *Appl. Phys. Lett.*, vol. **107**, p. 091106, 2015.
48. Li, N., Han, K., Spratt, W., Bedell, S., Ott, J., Hopstaken, M., Libsch, F., Li, Q., and Sadana, D., Ultra-Low-Power Sub-Photon-Voltage High-Efficiency Light-Emitting Diodes, *Nat. Photonics*, vol. **13**, pp. 588–592, 2019.
49. Sadi, T., Radevici, I., Kivisaari, P., and Oksanen, J., Electroluminescent Cooling in III–V Intracavity Diodes: Efficiency Bottlenecks, *IEEE Transact. Electron Dev.*, vol. **66**, pp. 2651–2656, 2019.
50. Krames, M.R., Shchekin, O.B., Mueller-Mach, R., Mueller, G.O., Zhou, L., Harbers, G., and Craford, M.G., Status and Future of High-Power Light-Emitting Diodes for Solid-State Lighting, *J. Disp. Technol.*, vol. **3**, pp. 160–175, 2007.
51. Xiao, P.T. and Yablonovitch, E., Ultra-High Luminescence Efficiency as a Technology Enabler: Solar Cells, Thermophotovoltaics, and Optoelectronic Refrigerators, *Proc. SPIE*, vol. 10758, p. 107580H, 2018.
52. Miller, O.D., Yablonovitch, E., and Kurtz, S.R., Strong Internal and External Luminescence as Solar Cells Approach the Shockley–Queisser Limit, *IEEE J. Photovolt.*, vol. **2**, pp. 303–311, 2012.
53. Fan, S., Villeneuve, P.R., Joannopoulos, J.D., and Schubert, E.F., High Extraction Efficiency of Spontaneous Emission from Slabs of Photonic Crystals, *Phys. Rev. Lett.*, vol. **78**, pp. 3294–3297, 1997.
54. Wiesmann, C., Bergenek, K., Linder, N., and Schwarz, U.T., Photonic Crystal LEDs – Designing Light Extraction, *Laser Photonics Rev.*, vol. **3**, pp. 262–286, 2009.
55. Radevici, I., Tiira, J., Sadi, T., Ranta, S., Tukiainen, A., Guina, M., and Oksanen, J., Thermophotonic Cooling in GaAs based Light Emitters, *Appl. Phys. Lett.*, vol. **114**, p. 051101, 2019.
56. Hsu, W.-C., Tong, J.K., Liao, B., Huang, Y., Boriskina, S.V., and Chen, G., Entropic and Near-Field Improvements of Thermoradiative Cells, *Sci. Rep.*, vol. **6**, p. 34837, 2016.
57. Liao, T., Zhang, X., Chen, X., Lin, B., and Chen, J., Negative Illumination Thermoradiative Solar Cell, *Opt. Lett.*, vol. **42**, pp. 3236–3238, 2017.
58. Tervo, E., Bagherisereshki, E., and Zhang, Z., Near-Field Radiative Thermoelectric Energy Converters: A Review, *Front. Energy*, vol. **12**, pp. 5–21, 2018.
59. Liao, T., Yang, Z., Chen, X., and Chen, J., Thermoradiative–Photovoltaic Cells, *IEEE Transact. Electron Dev.*, vol. **66**, pp. 1386–1389, 2019.
60. Liao, T., Zhang, X., Yang, Z., Chen, X., and Chen, J., Near-Field Thermoradiative Electron Device, *IEEE Transact. Electron Dev.*, vol. **66**, pp. 3099–3102, 2019.
61. Santhanam, P. and Fan, S., Thermal-to-Electrical Energy Conversion by Diodes under Negative Illumination, *Phys. Rev. B*, vol. **93**, p. 161410, 2016.

62. Ono, M., Santhanam, P., Li, W., Zhao, B., and Fan, S., Experimental Demonstration of Energy Harvesting from the Sky Using the Negative Illumination Effect of a Semiconductor Photodiode, *Appl. Phys. Lett*., vol. **114**, p. 161102, 2019.
63. Green, M.A., Third Generation Photovoltaics: Ultra-High Conversion Efficiency at Low Cost, *Prog. Photovolt.: Res. Appl*., vol. **9**, pp. 123–135, 2001.
64. Wedlock, B.D., Thermo-Photo-Voltaic Energy Conversion, *Proc. IEEE*, vol. **51**, pp. 694–698, 1963.
65. Swanson, R.M., A Proposed Thermophotovoltaic Solar Energy Conversion System, *Proc. IEEE*, vol. **67**, pp. 446–447, 1979.
66. Rephaeli, E. and Fan, S., Absorber and Emitter for Solar Thermo-Photovoltaic Systems to Achieve Efficiency Exceeding the Shockley-Queisser Limit, *Opt. Express*, vol. **17**, pp. 15145–15159, 2009.
67. Chan, W.R., Bermel, P., Pilawa-Podgurski, R.C.N., Marton, C.H., Jensen, K.F., Senkevich, J.J., Joannopoulos, J.D., Soljačić, M., and Celanovic, I., Toward High-Energy-Density, High-Efficiency, and Moderate-Temperature Chip-Scale Thermophotovoltaics, *Proc. Natl. Acad. Sci. USA*, vol. **110**, pp. 5309–5314, 2013.
68. Lenert, A., Bierman, D.M., Nam, Y., Chan, W.R., Celanovic, I., Soljacic, M., and Wang, E.N., A Nanophotonic Solar Thermophotovoltaic Device, *Nat. Nanotechnol*., vol. **9**, pp. 126–130, 2014.
69. Bierman, D.M., Lenert, A., Chan, W.R., Bhatia, B., Celanović, I., Soljačić, M., and Wang, E.N., Enhanced Photovoltaic Energy Conversion Using Thermally Based Spectral Shaping, *Nat. Energy*, vol. **1**, p. 16068, 2016.
70. Zhou, Z., Sakr, E., Sun, Y., and Bermel, P., Solar Thermophotovoltaics: Reshaping the Solar Spectrum, *Nanophotonics*, vol. **5**, pp. 1–21, 2016.
71. Omair, Z., Scranton, G., Pazos-Outn, L.M., Xiao, T.P., Steiner, M.A., Ganapati, V., Peterson, P.F., Holzrichter, J., Atwater, H., and Yablonovitch, E., Ultraefficient Thermophotovoltaic Power Conversion by Band-Edge Spectral Filtering, *Proc. Natl. Acad. Sci. USA*, vol. **116**, pp. 15356–15361, 2019.
72. Narayanaswamy, A. and Chen, G., Surface Modes for Near-Field Thermophotovoltaics, *Appl. Phys. Lett*., vol. **82**, pp. 3544–3546, 2003.
73. Laroche, M., Carminati, R., and Greffet, J.J., Near-Field Thermophotovoltaic Energy Conversion, *J. Appl. Phys*., vol. **100**, p. 063704, 2006.
74. Park, K., Basu, S., King, W.P., and Zhang, Z.M., Performance Analysis of Near-Field Thermophotovoltaic Devices Considering Absorption Distribution, *J. Quant. Spectrosc. Radiat. Transf.*, vol. **109**, pp. 305–316, 2008.
75. Ilic, O., Jablan, M., Joannopoulos, J.D., Celanovic, I., and Soljačić, M., Overcoming the Black Body Limit in Plasmonic and Graphene Near-Field Thermophotovoltaic Systems, *Opt. Express*, vol. **20**, pp. A366–A384, 2012.
76. Fiorino, A., Zhu, L., Thompson, D., Mittapally, R., Reddy, P., and Meyhofer, E., Nanogap Near-Field Thermophotovoltaics, *Nat. Nanotechnol*., vol. **13**, pp. 806–811, 2018.
77. Harder, N.P. and Green, M.A., Thermophotonics, *Semicond. Sci. Technol.*, vol. **18**, pp. S270–S278, 2003.
78. Buckner, B.D. and Heeg, B., Power Generation by Thermally Assisted Electroluminescence: Like Optical Cooling, but Different, *Proc. SPIE*, vol. **6907**, p. 69070I, 2008.

79. Zhao, B., Santhanam, P., Chen, K., Buddhiraju, S., and Fan, S., Near-Field Thermophotonic Systems for Low-Grade Waste Heat Recovery, *Nano Lett.*, vol. **18**, pp. 5224–5230, 2018.
80. McSherry, S., Burger, T., and Lenert, A., Effects of Narrowband Transport on Near-Field and Far-Field Thermophotonic Conversion, *J. Photonics Energy*, vol. **9**, p. 032714, 2019.
81. Heeg, B., Wang, J.-B., Johnson, S.R., Buckner, B.D., and Zhang, Y.-H., Thermally Assisted Electroluminescence: A Viable Means to Generate Electricity from Solar or Waste Heat, *Proc. SPIE*, vol. **6461**, p. 64610K, 2007.
82. He, R., Kraemer, D., Mao, J., Zeng, L., Jie, Q., Lan, Y., Li, C., Shuai, J., Kim, H.S., Liu, Y., Broido, D., Chu, C.-W., Chen, G., and Ren, Z., Achieving High Power Factor and Output Power Density in P-Type Half-Heuslers $Nb_{1-x}Ti_xFeSb$, *Proc. Natl. Acad. Sci. USA*, vol. **113**, pp. 13576–13581, 2016.
83. Zhao, B., Buddhiraju, S., Santhanam, P., Chen, K., and Fan, S., Self-Sustaining Thermophotonic Circuits, *Proc. Natl. Acad. Sci. USA*, vol. **116**, pp. 11596–11601, 2019.